Chapter 6

Fluorescence Detection of Nitroexplosive 2,4,6-Trinitrophenol by Pyridinium-based Chemosensor in Pure Aqueous Medium

6.1 Introduction

Detection of poisonous and explosive organic molecules with accurate selectivity and sensitivity is of primary concern in recent years for environmental protection, human health, and security. Energetic materials especially nitroaromatic compounds (NACs) are one of the major classes of pollutants [1-2]. NACs are important industrial intermediates and raw materials used in various manufacturing processes. Their extensive use in the synthesis of diverse products including pesticides, polymers, dyes, and military explosives contaminates soil and groundwater [3-4]. Several surveys conducted to study the level of explosives in soil and water resources, near military bases and NAC manufacturing industries confirms their elevated amounts [5-6]. Some selective examples of explosive NACs are given in **Figure 6.1**.

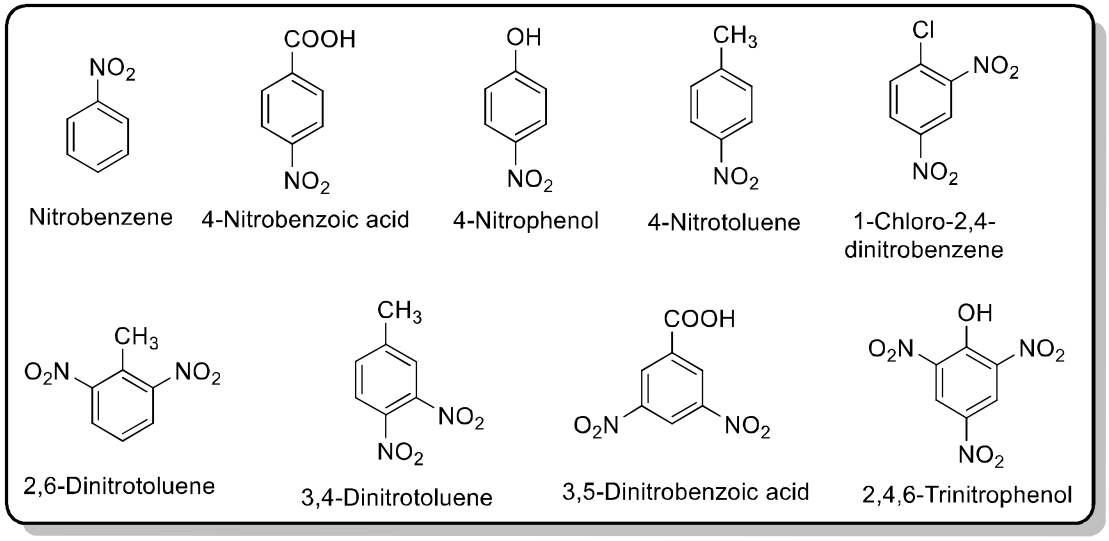

Figure 6.1 Examples of explosive nitroaromatic compounds

2,4,6-Trinitrophenol (TNP) commonly known as picric acid is a yellow crystalline solid and its salts are the major components of explosive formulations like Pentolite, Explosive D and Yellow D. TNP is also used in dye industries, leather processing, pharmaceuticals, mine fillings and in chemical labs [7-8]. It possesses high water solubility and violent explosive nature that easily contaminates air, soil, and water leading to severe health effects on living beings. The wastewater containing TNP from industries increases the risk of explosions as TNP forms shock-sensitive salts by reacting with metals and concrete (present in the drainage system and effluent treatment facilities) [9-10]. With direct exposure, TNP may cause many diseases such as vertigo, anemia, myalgia, yellow colouration of the skin, hematuria, albuminuria, destruction of erythrocytes, hemorrhagic nephritis, hepatitis, cancer, and

cyanosis [11-12]. TNP shows its adverse effect on plants by inhibiting photosynthetic electron transport in Photosystem II [13]. Due to its adverse effects on the environment and the biological system, it is highly desirable to develop sensitive methods for its detection. Various detection techniques have been developed in recent decades including colorimetry, mass and ion mobility spectrometry, and electrochemical sensing [14-15]. The deficit in selectivity, high cost, and portability issues limit the on-site use of these detection techniques. However, fluorescence-based detection techniques have advantages of excellent sensitivity, great selectivity, simple handling, portability, fast response, and facile sample preparation [16-17].

Most of the NACs have electron-deficient nature which makes them efficient quenchers of fluorescence and considerable interest has been paid for the development of fluorescent chemosensors [18-22]. When a fluorophore and quencher come in contact, quenching occurs due to diffusive collision (dynamic quenching) or complex formation (static quenching) (**Figure 6.2**).

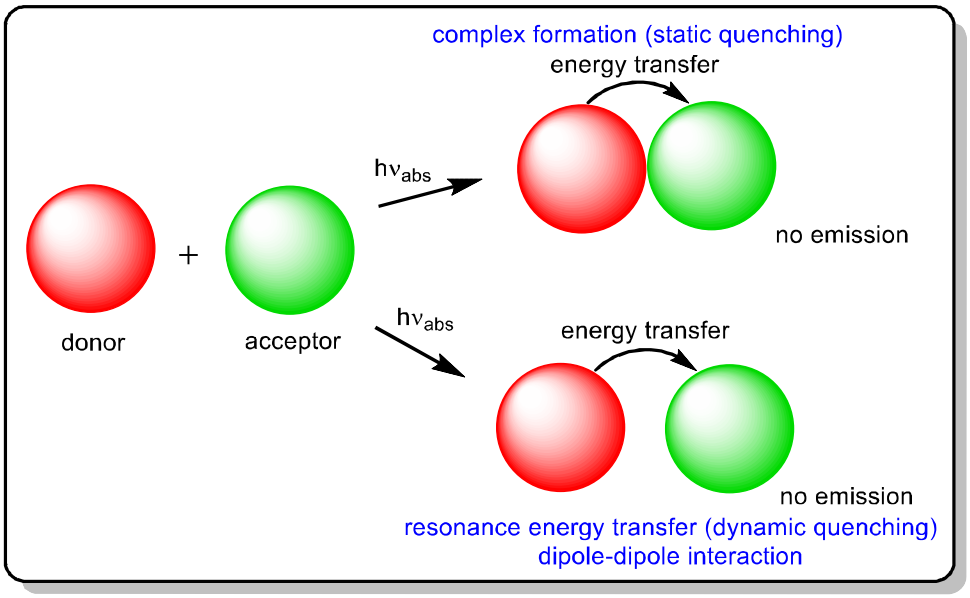

Figure 6.2 Mechanism of static and dynamic quenching

These processes can be differentiated by time-resolved experiments, in static quenching, the formation of the fluorophore-quencher complex takes place in the ground state and the decay in fluorescence lifetime of material remains unaffected on changing the quencher concentration. For dynamic quenching, the photoexcited fluorophore collides with an analyte molecule that results in a decrease in its fluorescence lifetime. A careful examination of the absorption spectra, after and before quencher addition is another approach to differentiate

between static and dynamic quenching. Dynamic quenching is an excited state phenomenon of a fluorophore and does not affect the absorption pattern whereas, in static quenching due to the complex formation in the ground state, changes in the absorption spectrum are observed (**Figure 6.3a**). The fluorescence of fluorophore can be quenched by both mechanisms (static and dynamic) with the same quencher [23-24]. Resonance energy transfer (RET), a part of dynamic quenching is an excited state process that involves the transfer of the excess energy of an excited molecule (donor) to an acceptor molecule and as a consequence, the emission intensity of donor gets quenched. The extent of the RET process can be predicted by studying the absorption spectrum of the acceptor (quencher) which overlaps with the emission spectrum of the donor (fluorophore) as depicted in **Figure 6.3b**. The donor and acceptor are coupled by a dipole-dipole interaction, the Förster distances R_0 (the molecular distance at which energy transfer is 50% efficient) are typically in the range of 10-100 Å [25-26].

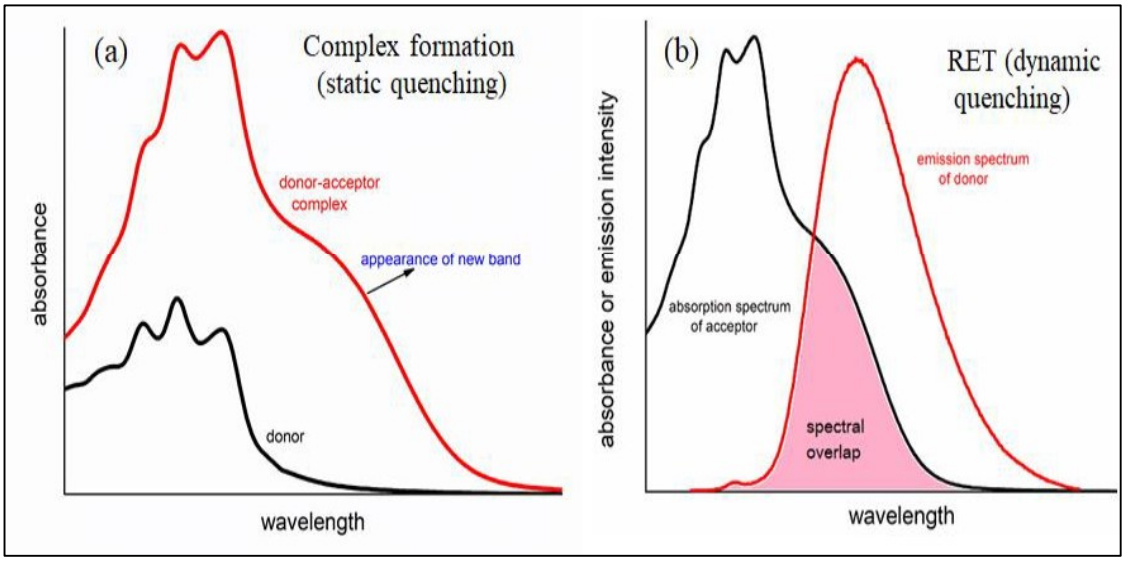

Figure 6.3 Pictorial representation of (**a**) ground-state complex formation (static quenching) (**b**) RET (dynamic quenching)

A variety of π electron-rich fluorescent organic molecules [27-29], oligomers/conjugated polymers [30-32], metal-organic framework [33], metal complexes [34-36], quantum dots [37-38], carbon dots [39-40], nanoaggregates [41-42], self-assemblies [43-44], etc. have been employed as chemosensors for TNP detection based on fluorescence quenching phenomenon. Some selected examples of chemosensors are given in **Figure 6.4**.

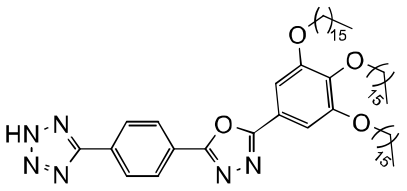

Detection limit = 700 ppt [45]
Sensing solvent = DMSO

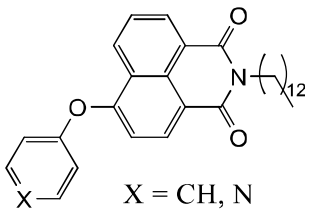

X = CH, N

Detection limit = 0.644 μM [46]
Sensing solvent = CH_3CN

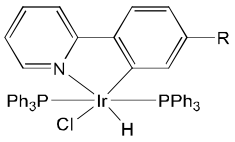

R = H, CHO

Detection limit = 264 nM and 65 nM [47]
Sensing solvent = THF- H_2O (v/v = 1 : 9)

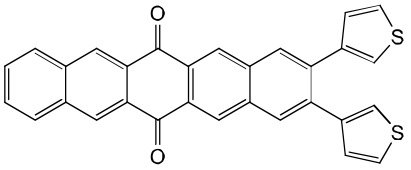

Detection limit = 500 ppb [48]
Sensing solvent = THF-H_2O (v/v = 1 : 9)

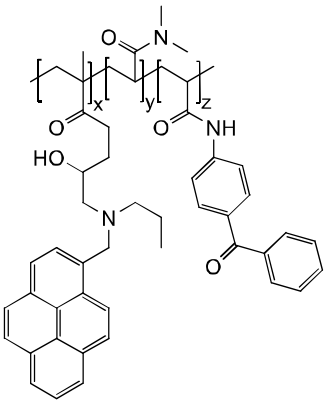

Detection limit = 56 μM [49]
Sensing solvent = H_2O

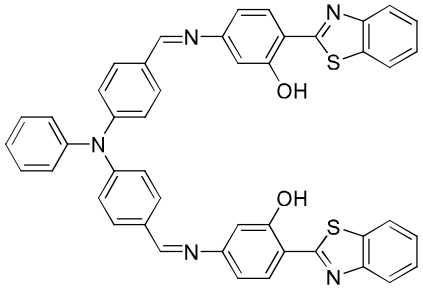

Detection limit = 2.94 ppb [50]
Sensing solvent = THF-H_2O (v/v = 1 : 9)

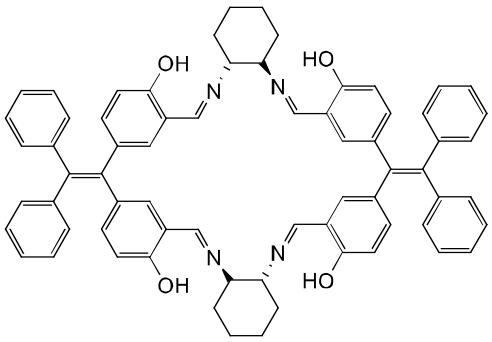

Detection limit = 23 ppm [51]
Sensing solvent = THF-H_2O (v/v = 1 : 9)

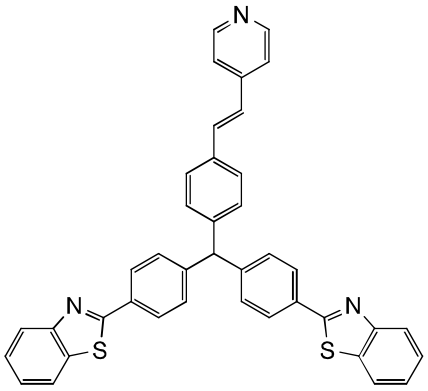

Detection limit = 23 ppm [52]
Sensing solvent = MeOH-H_2O (v/v = 8 : 2)

Figure 6.4 Selected examples of fluorescent chemosensors for TNP detection

The tedious synthesis and poor water solubility most of these chemosensors restrict their practical utility in natural water sources and industrial effluents dealing with TNP contamination. The solubility of chemosensor can be tuned by using imidazolium-, benzimidazolium- and pyridinium-based moieties [53-55]. For effective monitoring of nitroexplosives imidazolium- and benzimidazolium-based chemosensors have been reported in the organic, aqueous, and semi-aqueous medium.

Iyer and coworkers developed an imidazolium-based cationic conjugated polyelectrolyte **1** (**Figure 6.5**) for TNP detection. The imidazolium groups attached to side-chain provided good solubility in aqueous media and specific target site for desirable electrostatic interaction. The selectivity of **1** for TNP was explained *via* ground state charge transfer and RET phenomenon. The method was extended for TNP detection on a solid platform using paper strips and chitosan films [56]. Ding *et al*. studied the effect of surfactant micelles on the photophysical properties of a cationic bispyrene fluorophore **2** (**Figure 6.5**). The UV-visible absorption, steady-state fluorescence emission, quantum yield, fluorescence lifetime, and time-resolved emission spectra revealed that the cationic **2** was only encapsulated by the anionic sodium dodecyl sulfate (SDS) surfactant and exhibited on-off response towards TNP [57].

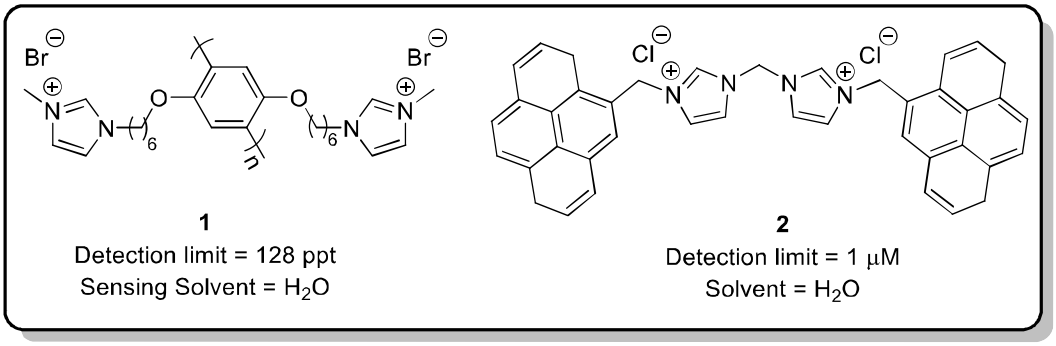

Figure 6.5 Imidazolium-based cationic conjugated polyelectrolyte (**1**) and cationic bispyrene (**2**) chemosensors

Mukherjee and coworkers synthesized two anthracene-functionalized fluorescent tris-imidazolium salts **3a** and **3b** (**Figure 6.6**) that selectively detected TNP in DMSO and DMSO-H_2O system. The crystal structures of **3a** and its TNP complex were successfully established by X-ray crystallography. TNP existed as picrate anion which on deprotonation resulted in quenching of fluorescence of **3a** [58].

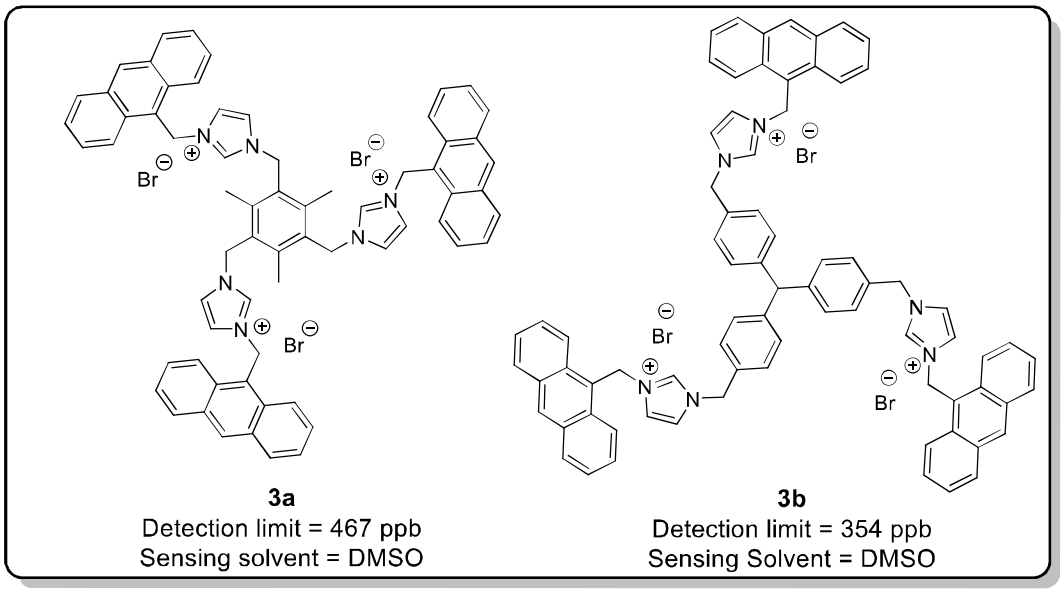

Figure 6.6 Imidazolium-based anthracene chemosensors (**3a** and **3b**)

Tian *et al*. synthesized a fluorescent imidazolium-based dansylamide chromophore **4** (**Figure 6.7**) which exhibited strong green fluorescence both in the solution and in the condensed phase. Sensor **4** exhibited a highly sensitive and selective response for TNP by strong electrostatic π-π interaction, the formation of a ground-state charge-transfer complex as well as the RET phenomenon [59]. Sakhuja and coworkers reported imidazolium- and benzimidazolium-based coumaryl sensors **5-c** (**Figure 6.7**) that were selective for nanomolar detection of TNP over other aromatic explosives in aqueous medium. Based on UV-visible studies, time-resolved fluorescence results, and DFT calculations it was suggested that high sensitivity of the sensors toward TNP was due to the ground-state charge-transfer complex formation [60-61].

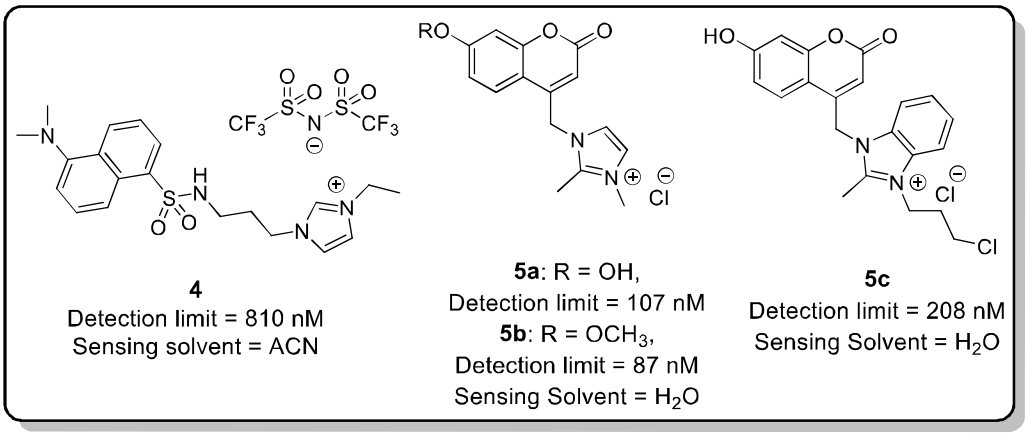

Figure 6.7 Imidazolium-based dansylamide (**4**) and coumarin (**5a-c**) chemosensors

Kumar and coworkers reported two imidazolium- and benzimidazolium-based tricationic tripods sensors **6a** and **6b** (**Figure 6.8**) for selective sensing of TNP in H_2O-DMSO mixture. In ^1H NMR study, the upfield shift of TNP protons suggested encapsulation of TNP in the cavity of the chemosensors. Thin films of **6a** showed fluorescence quenching in the presence of TNP vapours either from solid TNP or from aqueous saturated solution of TNP in less than 120 seconds [62]. They also reported three imidazolium-based tripods **7a-c** (**Figure 6.8**) possessing alkoxy chains on the biphenyl units and investigated the effect of chain length on their ease in aggregation and efficiency in detection of nitroaromatic compounds. Tripods **7b** and **7c** self-assembled to form dense nano-spheres but **7a** having shorter *n*-butyl alkyl chains was unable to aggregate. Among these three tripod chemosensors, **7b** showed superior selectivity towards TNP [63].

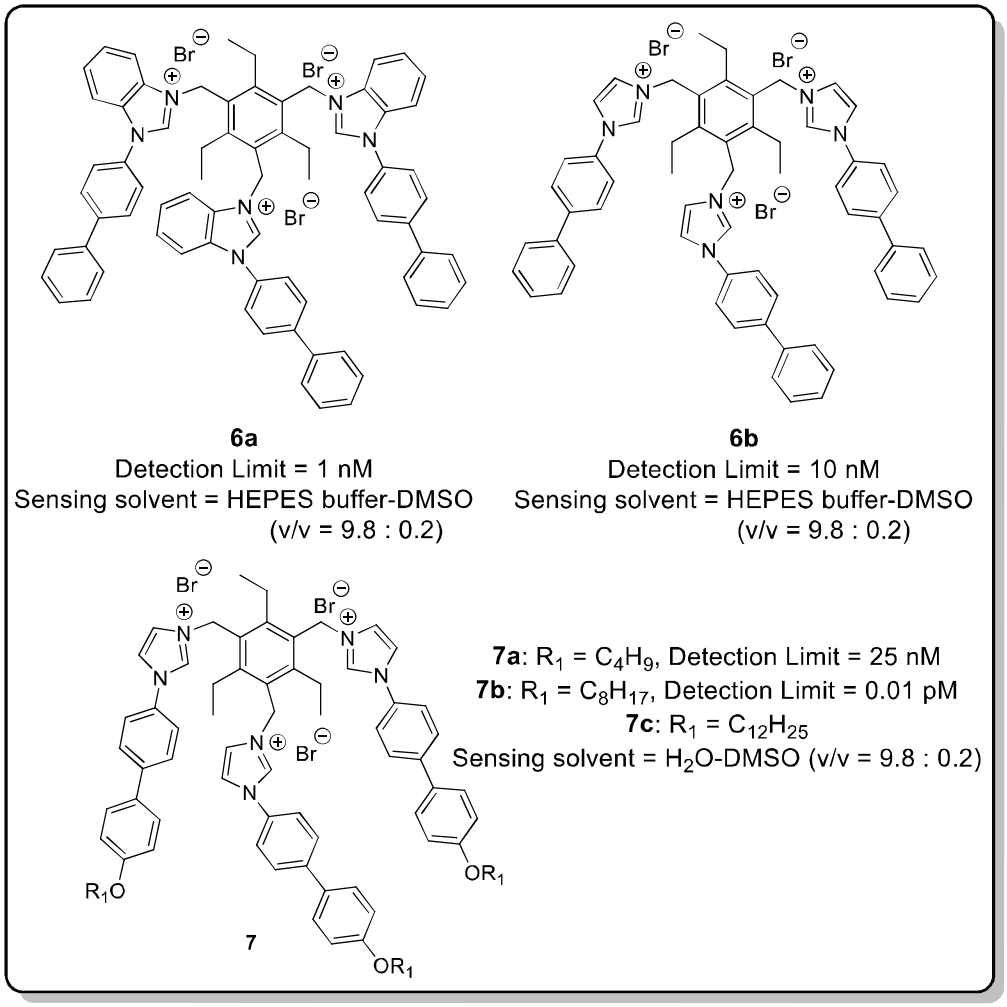

Figure 6.8 Imidazolium-based triethylbenzene **(6a-b**) and biphenyl (**7a-c**) chemosensors

Kumar and coworkers also reported that 1-(*p*-terphenyl)-benzimidazolium-based probe **8** (**Figure 6.9**), undergo self-assembly to form rod-like structures in aqueous medium. In the presence of increasing amounts of TNP, these aggregates showed an aggregation/disaggregation process before their dissolution to well-dispersed spheres. In the presence of TNP, superamplified fluorescence quenching of blue emission in both solution and solid-state was observed [64]. Synthesis of dansyl conjugated tripod **9** (**Figure 6.9**) was also reported by this group, which undergoes aggregation-induced emission enhancement in 98% aqueous medium. The aggregation was confirmed by dynamic light scattering and transmission electron microscopic studies. Probe **9** showed highly selective amplified quenching in fluorescence in the presence of TNP in the solution phase as well as on paper strips [65].

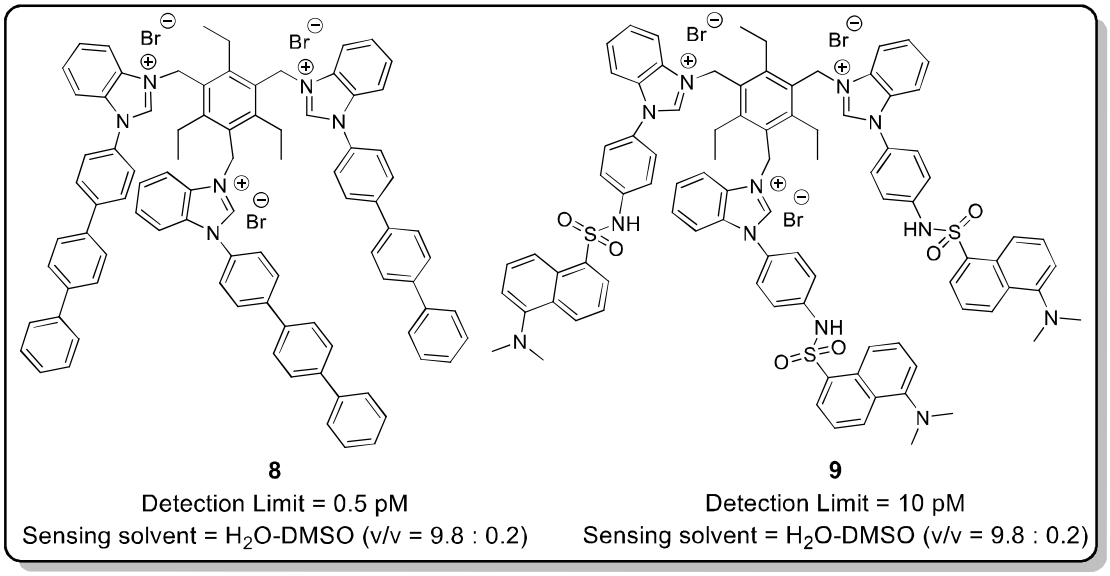

Figure 6.9 Benzimidazolium-based *p*-terphenyl (**8)** and dansyl (**9**) chemosensors

Pyridinium-based moieties are considered as privileged scaffolds due to their occurrence in many natural and bioactive compounds. Moreover, they show wide applications as dyes, cosmetics, surfactants, pharmaceuticals, catalysts, sensors, and electrolytes [66]. A few examples of pyridinium-based chemosensors for metal ions, anions, amino acids, and saccharides detection are shown in **Figure 6.10** [67-70].

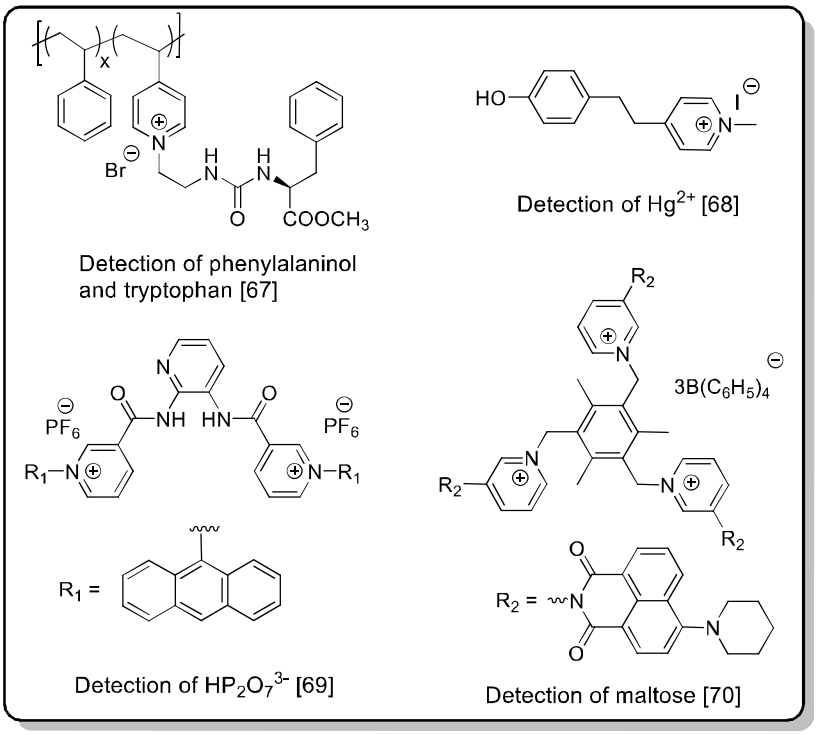

Figure 6.10 Selected examples of pyridinium-based chemosensors

Kumar and coworkers developed a pyridinium-dansyl conjugate based three-dimensional molecular probe **10** (**Figure 6.11**), which undergoes aggregation-induced emission in water with excellent fluorescence enhancement ($\Phi = 0.71$). It selectively detected TNP and showed dynamic quenching as observed from the increase in the life-time of **10**. DFT studies revealed that picrate anion places itself closer to the dansyl fluorophore due to its decreased cavity length thereby increasing the sensitivity of the probe [71].

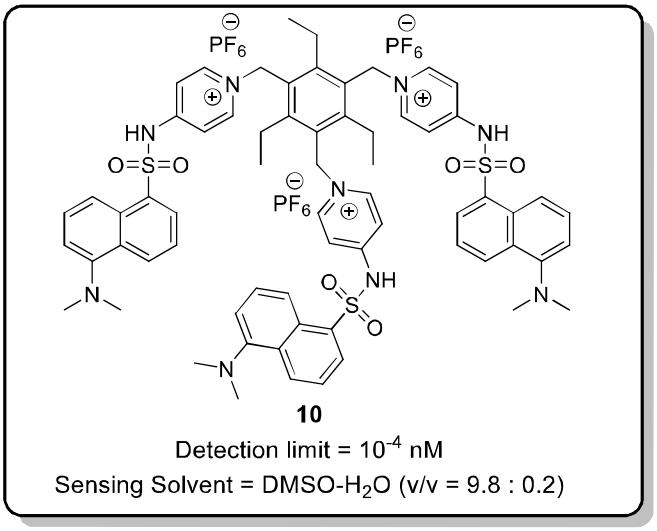

Figure 6.11 Pyridinium-based dansyl chemosensor (**10**)

In this chapter we envisioned the synthesis of pyridinium-based chemosensor **BZQZPy** and used its fluorescence behaviour for selective and sensitive detection of nitroexplosive TNP in pure aqueous medium.

6.2 Results and Discussion

6.2.1 Synthesis and Characterization of IPy and BZQZPy

To maintain a green environment for the detection of TNP, a water-soluble chemosensor **BZQZPy** was developed. The 1-(2-bromoethyl)-1H-indole-2,3-dione was synthesized according to the reported method [72]. Quaternization of 1-(2-bromoethyl)-1H-indole-2,3-dione with pyridine enhanced hydrophilicity in the moiety and provided **IPy**. To impart fluorescence characteristics, **IPy** was treated with *o*-phenylenediamine to afford **BZQZPy** (**Scheme 6.1**).

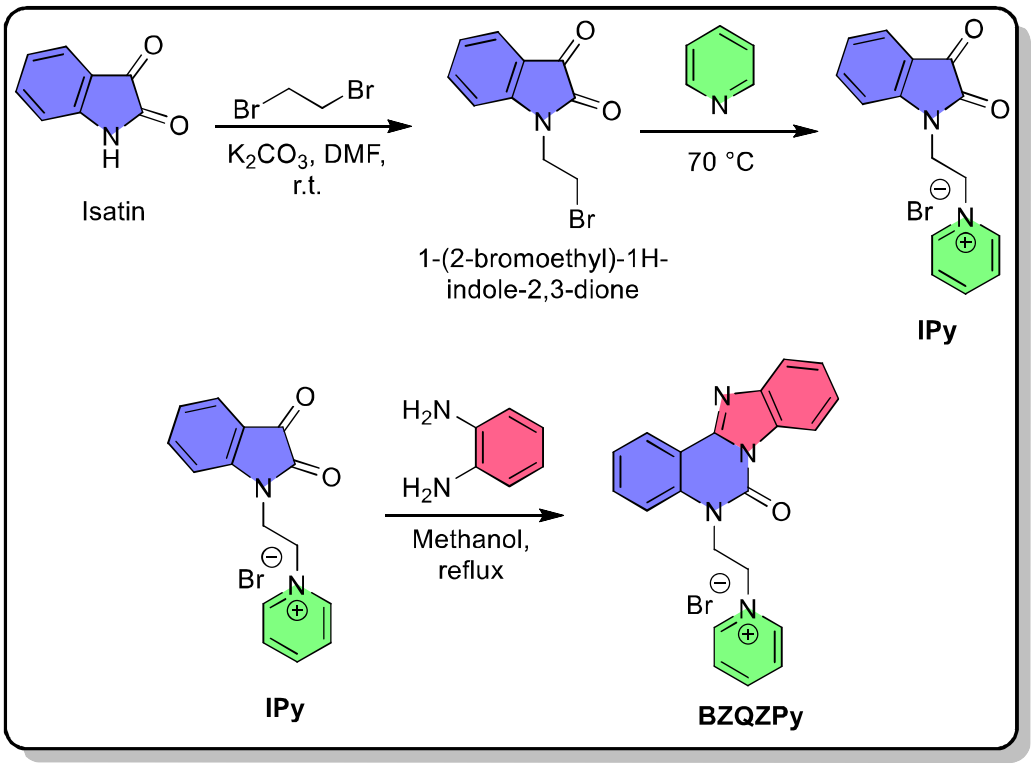

Scheme 6.1 Synthetic route of **BZQZPy**

The formation of synthesized **IPy** and **BZQZPy** was fully studied based on ^{1}H and ^{13}C NMR spectroscopy, HRMS, and X-ray crystallography.

In the ^{1}H NMR spectrum of **IPy**, the appearance of one doublet at 9.21 ppm and two triplets at 8.62 and 8.12 ppm for five pyridinium protons confirmed the quaternization of 1-(2-bromoethyl)-1H-indole-2,3-dione with pyridine. The two aliphatic protons were observed as triplets at 4.33 and 4.94 ppm and rest four aromatic protons appeared in the range 7.17-7.63 ppm (**Figure 6.12**).

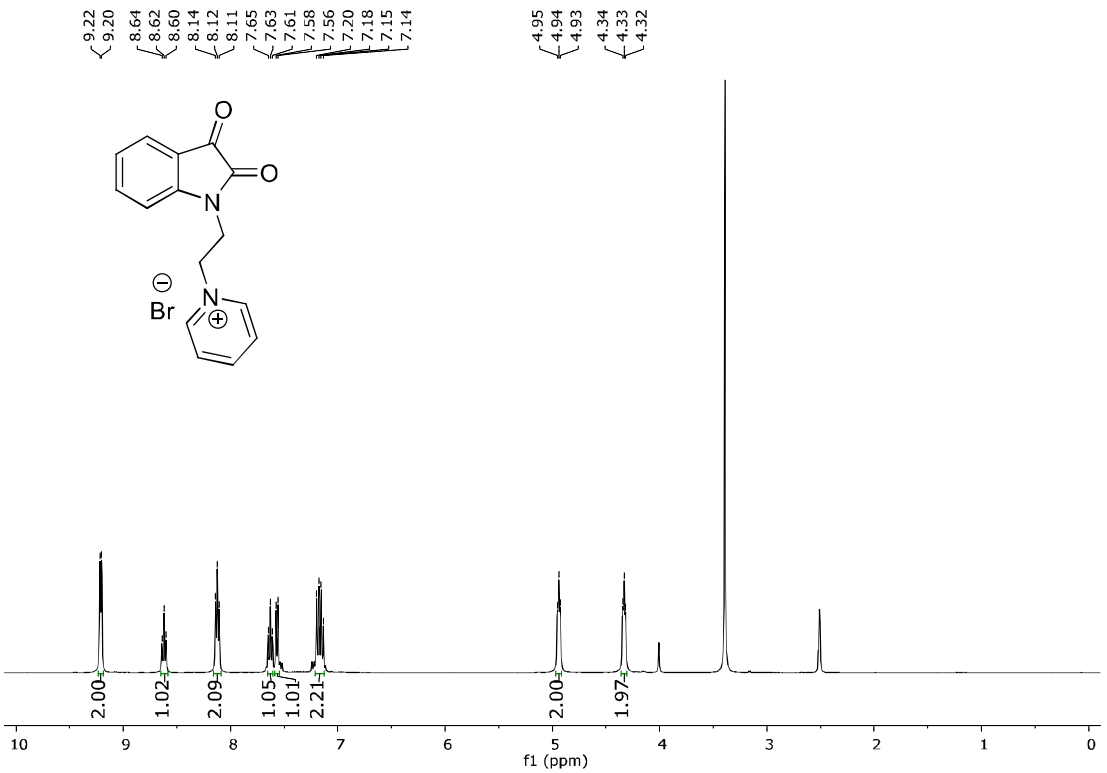

Figure 6.12 ^{1}H NMR Spectrum of **IPy** (DMSO-d_6)

In **BZQZPy**, there was a slight shift in the doublet and one of the triplets of pyridinium protons and the signals appeared at 9.15 and 8.60 ppm, respectively. The other pyridinium proton triplet merged with the signals of aromatic protons and all these proton signals were observed in the range 8.44-7.43 ppm. The aliphatic protons were observed as triplets at 5.10 and 4.94 ppm (**Figure 6.13**). The disappearance of the ketonic ^{13}C NMR signal at 182.9 ppm in **IPy** also confirmed the formation of **BZQZPy** (**Figure 6.14** and **Figure 6.15**).

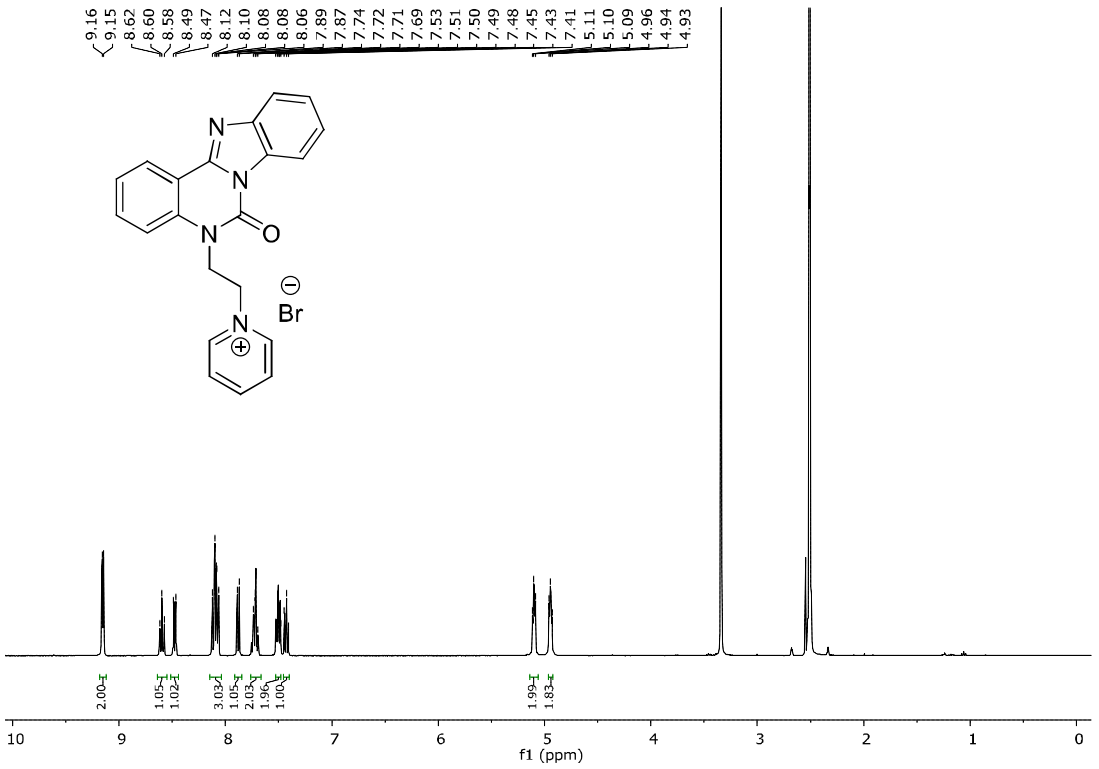

Figure 6.13 ^{1}H NMR Spectrum of **BZQZPy** (DMSO-d_6)

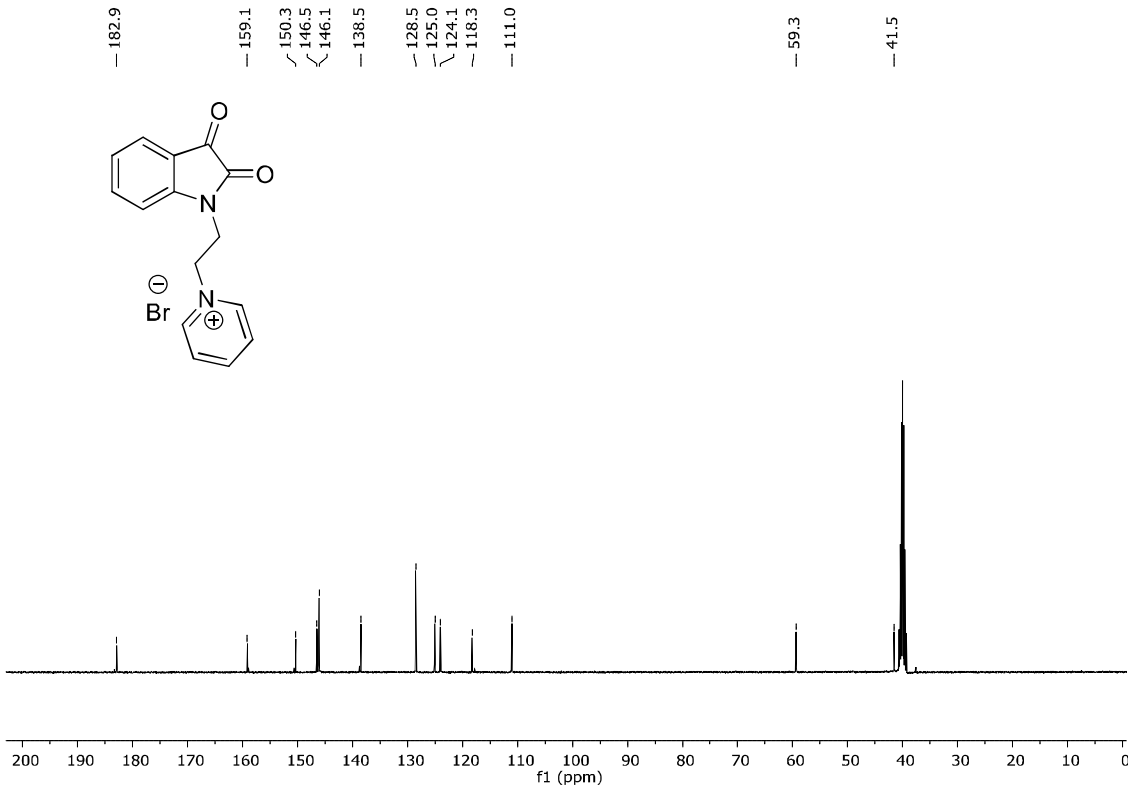

Figure 6.14 ^{13}C NMR Spectrum of **IPy** (DMSO-d_6)

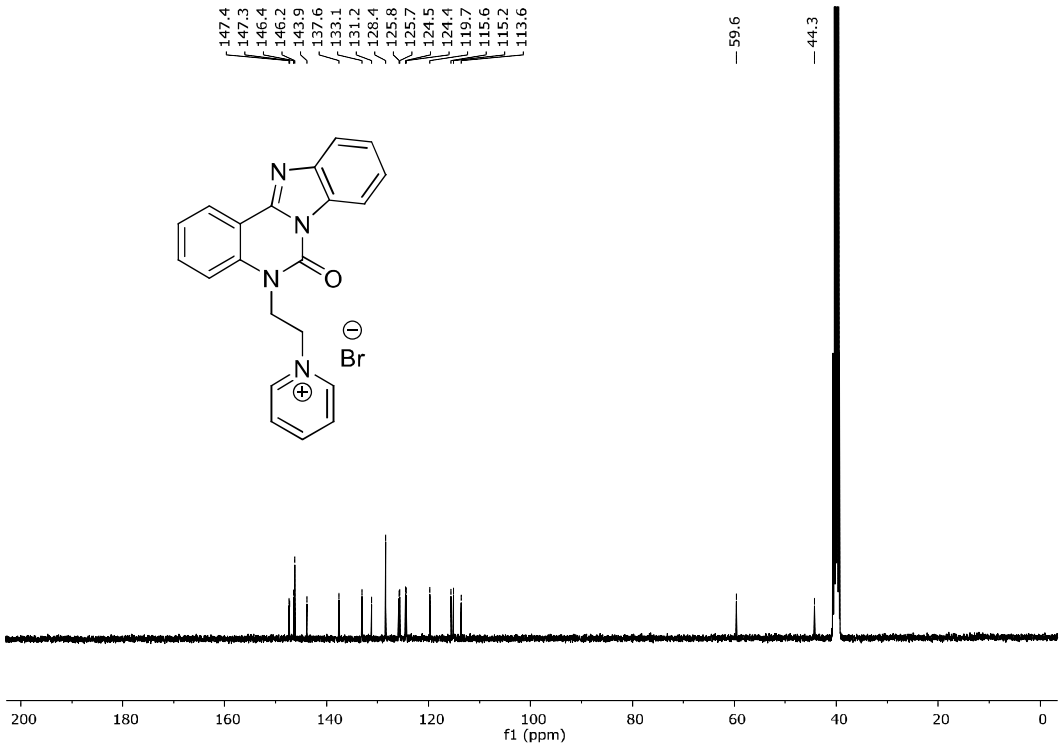

Figure 6.15 ^{13}C NMR Spectrum of **BZQZPy** (DMSO-d_6)

HRMS data showed the presence of [**IPy**-Br]$^+$ at *m/z* = 253.0967 (253.0972, calculated) and [**BZQZPy**-Br]$^+$ at *m/z* = 341.1388 (341.1397, calculated) (**Figure 6.16** and **Figure 6.17**).

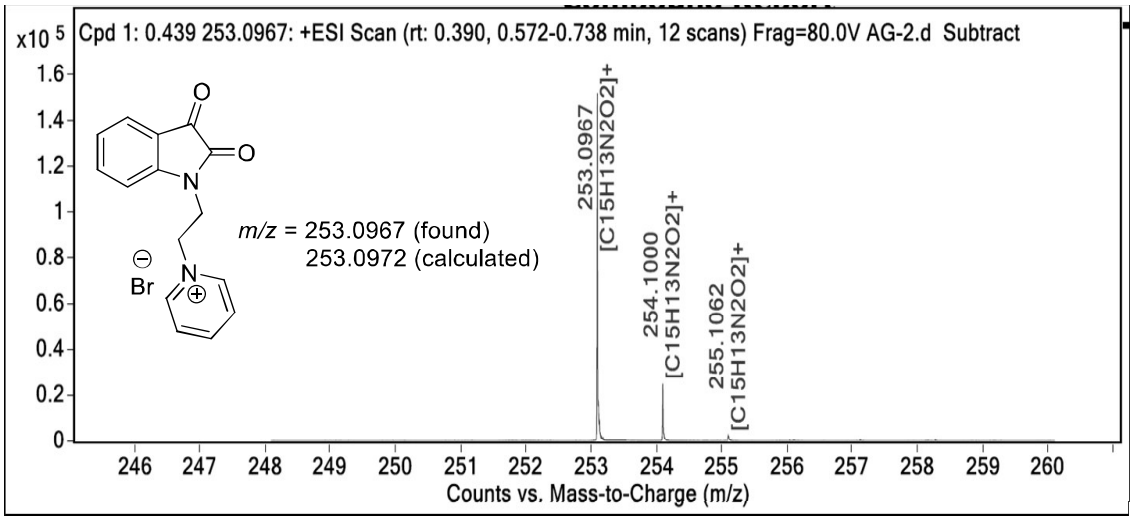

Figure 6.16 HRMS of **IPy**

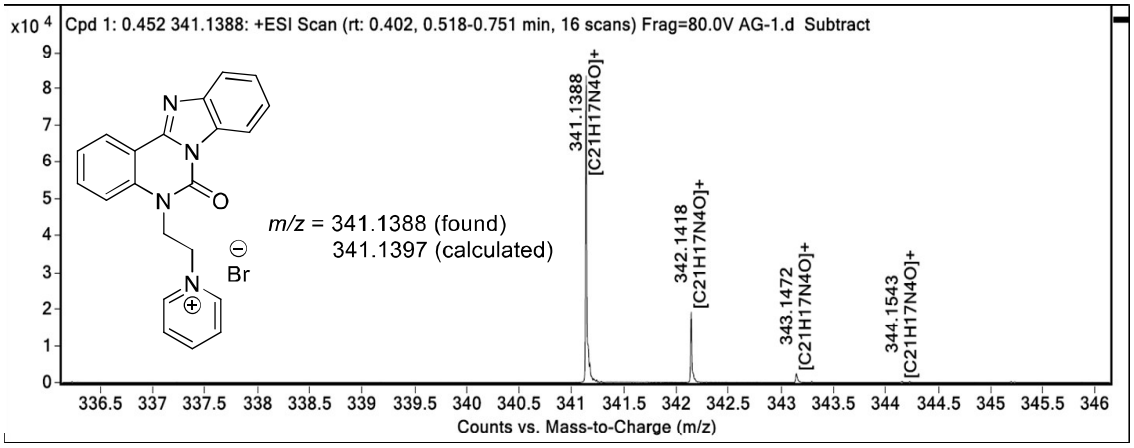

Figure 6.17 HRMS of **BZQZPy**

The structures of **IPy** and **BZQZPy** were further confirmed by single-crystal structure analysis. The single crystals of **IPy** and **BZQZPy** were obtained as yellowish-red and yellow coloured blocks, respectively from ethanol-ethyl acetate solvent mixture. The compound **IPy** with the molecular formula ($C_{15}H_{15}N_2O_3Br$) crystallized in the monoclinic $P2_1/c$ space group, which was composed of one organic molecular cation, one bromide anion, and one water solvent molecule. Similarly, the crystal structure of compound **BZQZPy** ($C_{21}H_{19}N_4O_2Br$) consisted of one organic molecular cation, one bromide counter anion, and one water molecule, but it crystallized in the triclinic *P*-1 space group. The single-crystal XRD data and cell parameters are summarized in **Table 6.1**.

Table 6.1 Single-crystal XRD data and structure refinement for **IPy** and **BZQZPy**

Identification code	**IPy**	**BZQZPy**
Empirical formula	$C_{15}H_{15}BrN_2O_3$	$C_{21}H_{19}BrN_4O_2$
Formula weight	351.20	439.31
Temperature/K	293	293
Crystal system	Monoclinic	triclinic
Space group	$P2_1/c$	*P*-1
a/Å	12.8355(5)	8.9282(5)
b/Å	9.4068(4)	10.3437(5)
c/Å	12.1461(4)	11.1616(6)
α/°	90	64.230(5)
β/°	98.939(4)	88.733(5)
γ/°	90	87.015(5)

Volume/Å^3	1448.72(10)	927.01(9)
Z	4	2
ρ_{calc}g/cm^3	1.610	1.574
μ/mm^{-1}	2.849	3.236
F(000)	712.0	448.0
Crystal size/mm^3	0.4 × 0.14 × 0.05	0.3 × 0.2 × 0.1
Radiation	MoKα (λ = 0.71073)	CuKα (λ = 1.54184)
2Θ range for data collection/°	6.634 to 62.236	8.798 to 148.62
Index ranges	-15 ≤ h ≤ 18, -12 ≤ k ≤ 13, -16 ≤ l ≤ 17	-11 ≤ h ≤ 9, -12 ≤ k ≤ 12, -13 ≤ l ≤ 13
Reflections collected	14049	8181
Independent reflections	4103 [R_{int} = 0.0315, R_{sigma} = 0.0297]	3558 [R_{int} = 0.0648, R_{sigma} = 0.0445]
Data/restraints/parameters	4103/1/193	3558/0/256
Goodness-of-fit on F^2	1.050	1.123
Final R indexes [I>=2σ (I)]	R_1 = 0.0488, wR_2 = 0.1170	R_1 = 0.0807, wR_2 = 0.2323
Final R indexes [all data]	R_1 = 0.0631, wR_2 = 0.1237	R_1 = 0.0822, wR_2 = 0.2330
Largest diff. peak/hole / e Å^{-3}	3.22/-2.02	2.62/-1.60

[a] $R_1 = \sum||F_o| - |F_c||/\sum|F_o|$. [b] $wR_2 = [\sum w(F_o^2 - F_c^2)^2/\sum w(F_o^2)^2]^{1/2}$, where $w = 1/[\sigma^2(F_o^2) + (aP)^2 + bP]$, $P = (F_o^2 + 2F_c^2)/3$.

The ORTEP diagrams of **IPy** and **BZQZPy** are illustrated in **Figure 6.18**. Four ionic molecules with four water of solvation are packed in a unit cell for **IPy** (**Figure 6.19a**). In the unit cell of **BZQZPy**, two ionic molecules with two water molecules are observed (**Figure 6.19b**).

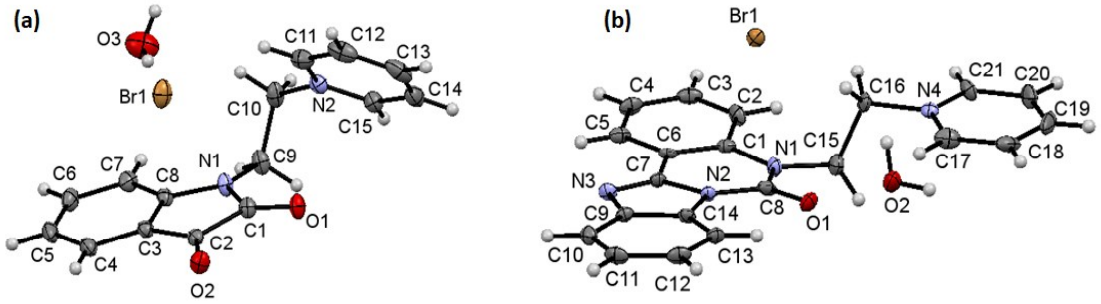

Figure 6.18 ORTEP diagram of (**a**) **IPy** and (**b**) **BZQZPy**. The crystal structures were drawn with 50% ellipsoidal probability

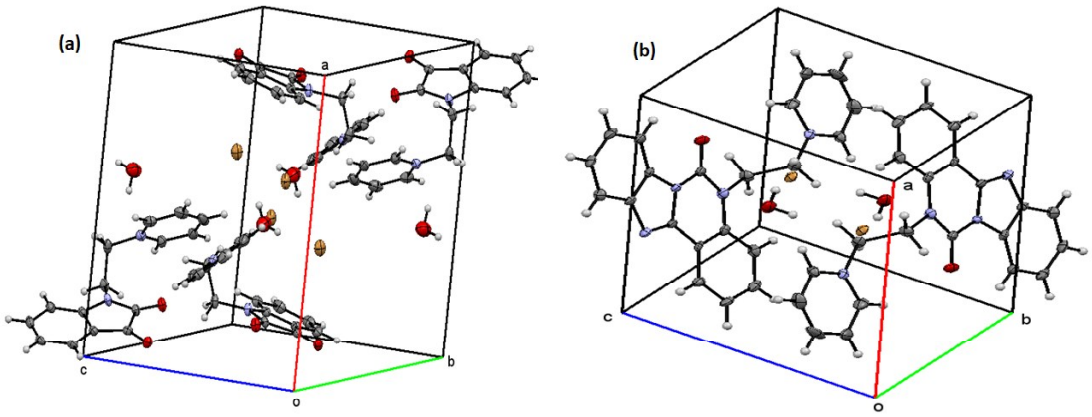

Figure 6.19 Unit cell packing of (**a**) **IPy** and (**b**) **BZQZPy**

In **IPy**, the indole-2,3-dione fused rings are essentially planar with C(7)–C(8)–N(1)–C(1) dihedral angle 179.87° (**Figure 6.20a**). The C(1)=O(1) and C(2)=O(2) groups both have bond lengths 1.213(4) Å. The C(1)–C(2) bond length is 1.559(4) Å, which is the longest covalent bond in this molecule. The C(9)-C(10) single bond length between the methylene group is 1.521(5) Å. The N(1)–C(1), N(1)–C(8) and N(1)–C(9) bond lengths, involving indole ring nitrogen atom, are 1.373(4), 1.418(4) and 1.456(4) Å, respectively. The N(2)–C(11), N(2)–C(15) and N(2)–C(10) bond lengths involving the pyridinium ring nitrogen atom are 1.349(4), 1.351(4) and 1.485(4) Å, respectively. The pyridinium ring plane is arranged 54.48° with respect to the indole ring plane. The C(1)–N(1)–C(8), C(1)–N(1)–C(9), C(8)–N(1)–C(9) bond angles are 110.9(2)°, 123.4(2)° and 124.6(2)°, respectively. For the pyridinium part, the C(11)–N(2)–C(15), C(11)–N(2)–C(10) and C(15)–N(2)–C(10) bond angles are 121.4(3)°, 120.4(3)° and 118.1(3)°, respectively.

The main tetracyclic benzimidazo-quinazolinone part of **BZQZPy** is nearly planar, benzimidazole ring is planar, while benzene ring plane (C(1)C(2)C(3)C(4)C(5)C(6) ring) of quinazolinone moiety is slightly deviated around 5.90° with respect to the benzimidazole ring plane (**Figure 6.20b**). The torsional angles C(1)–C(6)–C(7)–N(2), C(1)–C(6)–C(7)–N(3), C(5)–C(6)–C(7)–N(3), and C(5)-C(6)–C(7)–N(2) are 3.32°, -179.94°, 0.62°, and -176.12°, respectively. The pyridinium ring plane (N(4)C(17)C(18)C(19)C(20)C(21)) is arranged almost parallel with the benzimidazo-quinazolinone ring plane with 4.78° angle between the planes. The C(8)=O(1) bond distance is 1.230(10) Å. The benzimidazole ring N(3)–C(7), N(3)–C(9), N(2)–C(8), N(2)–C(7), N(2)–C(14) distances are 1.302(10), 1.405(10), 1.388(10), 1.399(10) and 1.401(10) Å, respectively. The N(1)–C(8), N(1)–C(1) and N(1)–C(15) bond

distances are 1.374(10), 1.422(10) and 1.467(10) Å, respectively. The pyridinium N(4)–C(21), N(4)–C(17), N(4)–C(16) bond distances are 1.342(10), 1.357(11) and 1.494(10) Å, respectively. The pyridinium N atom to methylene C atom bond distances in **IPy** and **BZQZPy**, respectively are 1.485(4) Å and 1.494(10) Å. The three-dimensional crystal packing structure of **BZQZPy** is stabilized by hydrogen bonding and non-covalent bond weak interactions. The O(2)–H(2A)·····Br(1) and O(2)–H(2B)·····N(3) hydrogen bond distances are 2.480 and 2.026 Å, respectively. The closest Br·····Br non-bonding distance is 6.400 Å for the **BZQZPy**.

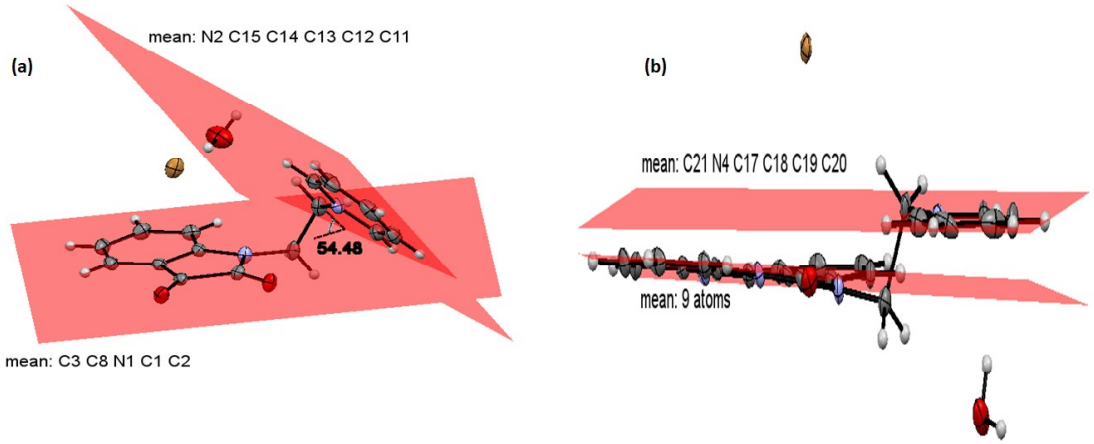

Figure 6.20 Ring plane diagrams of (**a**) **IPy** and (**b**) **BZQZPy**

6.2.2 Detection of analytes using BZQZPy in the pure aqueous medium

Figure 6.21 display photographs of **BZQZPy** with different organic analytes 1-chloro 2,4-dinitrobenzene (Cl-DNB), 4-nitrobenzoic acid (NBA), 4-nitrophenol (NP), 4-nitrotoluene (NT), 2,4-dinitrophenol (DNP), 3,4-dinitrotoluene (3,4-DNT), 3,5-dinitrobenzoic acid (DNBA), 3,5-dinitrotoluene (3,5-DNT), benzoic acid (BA), nitrobenzene (NB), nitromethane (NM), 2,4,6-trinitrophenol (TNP), *p*-cresol in water under 365 nm UV lamp. A bright cyan colour of **BZQZPy** remained unaffected in the presence of these analytes, but for TNP it diminished, which indicates that **BZQZPy** acts as a fluorescent turn-off chemosensor.

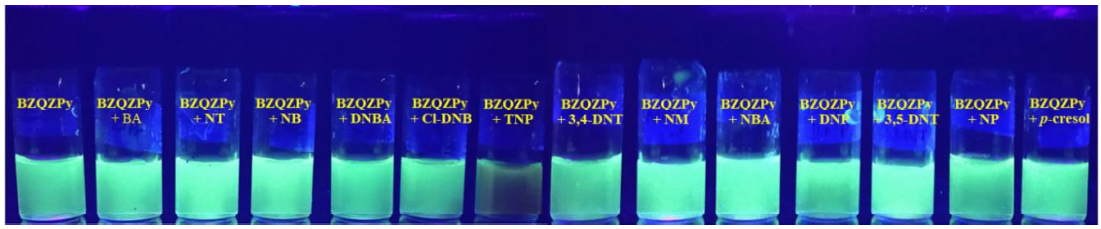

Figure 6.21 Photograph of the solution of **BZQZPy** (10^{-4} M) with organic analytes in water under a 365 nm UV lamp

The absorbance and fluorescence spectra were recorded in water. In the absorption spectrum of **BZQZPy**, three absorption bands at λ_{max} = 323 nm, 338 nm, and 357 nm were observed. **BZQZPy** showed good emissive nature (Φ = 0.30) in water and a strong emission maximum was observed at 512 nm (λ_{ex} = 375 nm) (**Figure 6.22**).

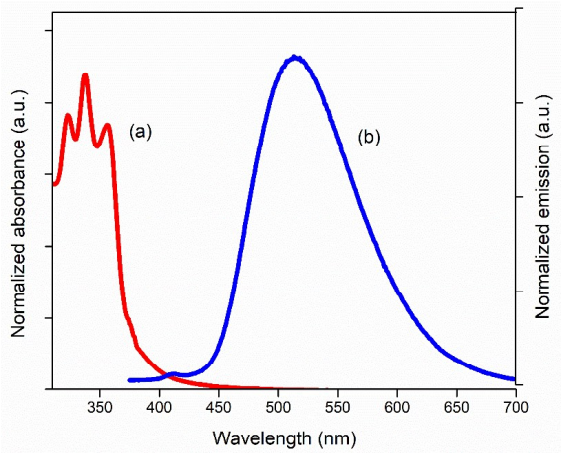

Figure 6.22 (**a**) UV-visible and (**b**) fluorescence spectra of **BZQZPy** (10^{-4} M) in water

The absorbance and fluorescence behaviour of **BZQZPy** was also studied in the presence of different organic analytes. No change was observed with most of these analytes, however, the addition of NP, DNP, and TNP showed an increase in the intensity of each absorption band and appearance of a new absorption band around 398 nm (**Figure 6.23a**). In the fluorescence spectra, an emission peak centred at 512 nm for **BZQZPy** was quenched on the addition of these three analytes, while maximum quenching was observed on TNP addition (**Figure 6.23b**).

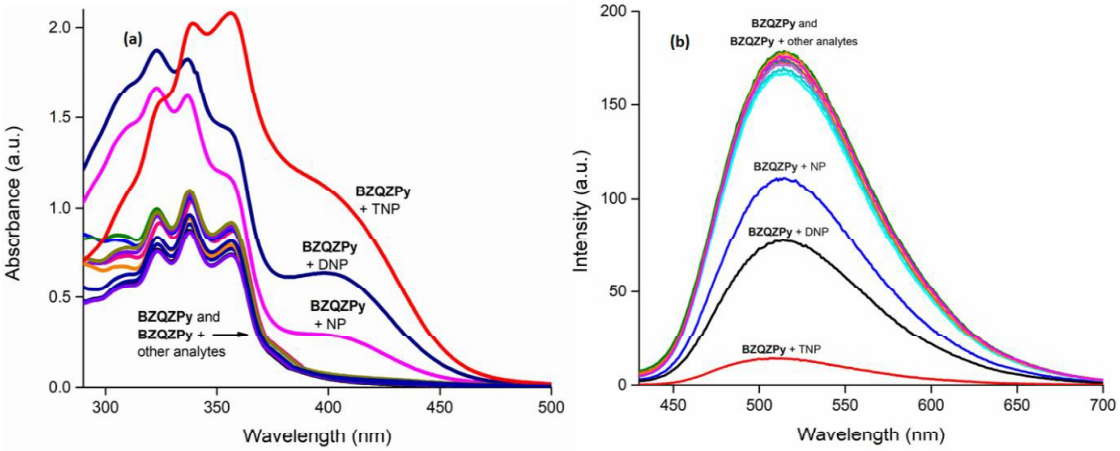

Figure 6.23 (**a**) Absorbance and (**b**) fluorescence response of **BZQZPy** (10^{-4} M) towards organic analytes in water

The sensing behaviour of **BZQZPy** for TNP was also tested in MeOH and DMSO. After TNP addition, the intensities of absorption bands for **BZQZPy** in MeOH (306 nm, 323 nm, and 337 nm) and DMSO (311, 324 nm and 340 nm) increased (**Figure 6.24a**). The appearance of two new absorption bands in MeOH (353 nm and 398 nm) and DMSO (379 nm and 437 nm) suggested the interaction of **BZQZPy** with TNP. **BZQZPy** showed emission peaks at 489 nm and 476 nm in MeOH and DMSO, respectively, and on TNP addition fluorescence quenching was observed (**Figure 6.24b**). Due to poor solubility of **BZQZPy** in less or non-polar solvents, the sensing study could not be performed in CH_3CN, $CHCl_3$, DCM, hexane, and toluene.

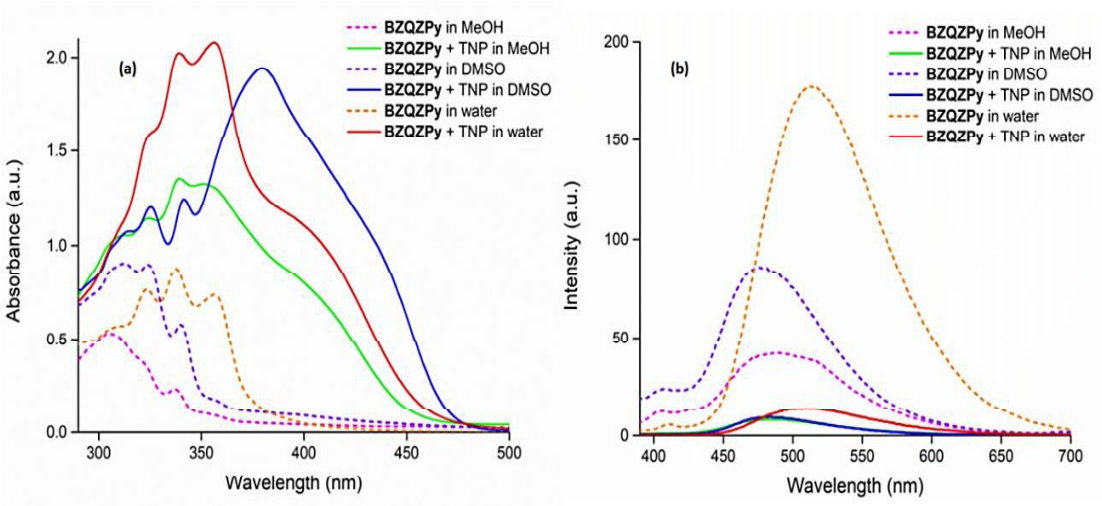

Figure 6.24 (**a**) Absorbance and (**b**) fluorescence response of **BZQZPy** (10^{-4} M) before and after TNP addition in different solvents

6.2.3 Binding interaction studies between BZQZPy and TNP

To study the interaction between **BZQZPy** (8×10^{-5} M) and TNP, a series of UV-visible and fluorescence titration experiments were carried out. On the gradual addition of TNP to the aqueous solution of **BZQZPy**, the intensity of each absorption band (323 nm, 338 nm, and 357 nm) increased (**Figure 6.25a**). Also, the appearance of new absorption bands at 398 nm suggested the formation of a ground state charge transfer complex between **BZQZPy** and TNP. In the fluorescence titration experiment, the intensity of peak at 512 nm gradually decreased on the incremental addition of TNP. This is due to the deprotonation of phenolic -OH of TNP in aqueous medium and subsequent anion exchange with **BZQZPy** (**Figure 6.25b**).

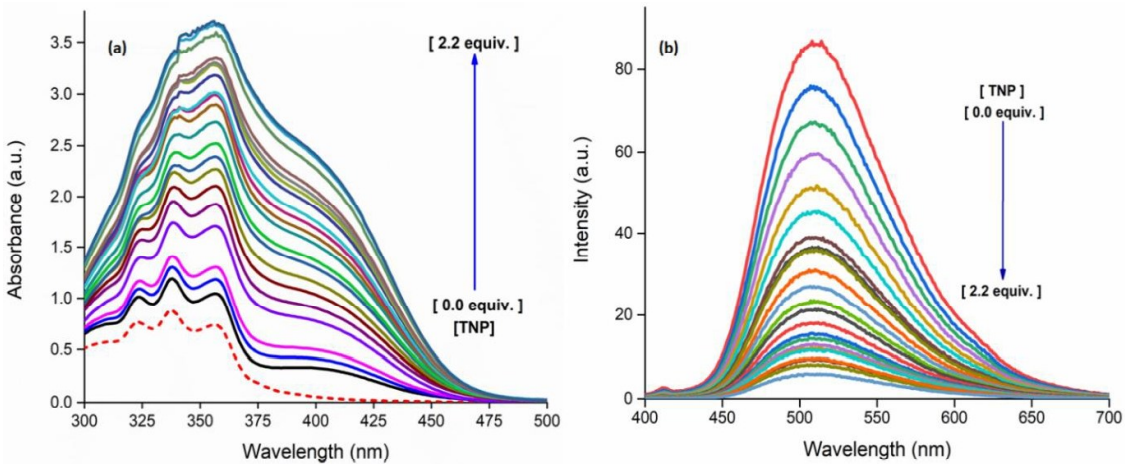

Figure 6.25 Titration spectra from (**a**) UV-visible and (**b**) fluorescence studies upon gradual addition of TNP to **BZQZPy**

The lower detection limit determined by the emission titrations was found to be 20 nM. It was calculated using the equation $3\sigma/K$, where σ is the standard deviation of 10 blank measurements, and K is the slope from the intensity versus sample concentration plot [50]. To investigate the quenching efficiency of **BZQZPy**, the Stern-Volmer Quenching constant (K_{SV}) was calculated by plotting fluorescence intensity ratio (I_0/I-1) against the concentration of TNP (**Figure 6.26**). The value of K_{SV} = 1.53 x 10^4 M^{-1} implied a high sensitivity of **BZQZPy** towards TNP. The Stern-Volmer plot showed two regions, at lower concentrations of TNP, a linear variation due to static quenching is observed. At higher concentrations due to the dynamic quenching, this linearity deviates and increases nearly exponentially.

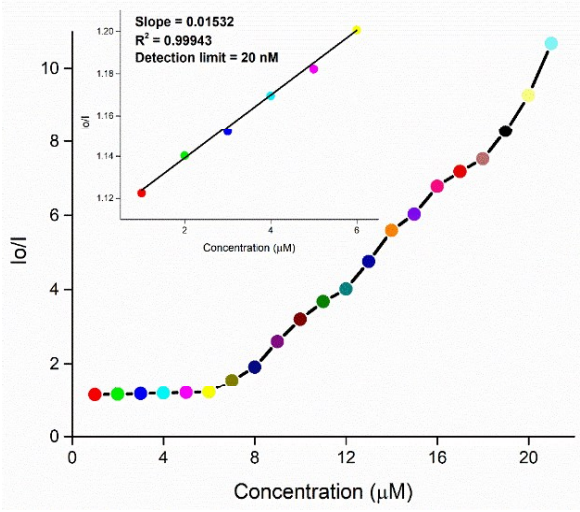

Figure 6.26 Stern-Volmer Plots in the response to increasing concentration of TNP in aqueous media. Inset: The Stern-Volmer plot at the lower concentration of TNP

The formation of ground-state charge transfer complex was further confirmed by density functional theory (DFT) calculations. The energy-optimized structures of cationic **BZQZPy**$^+$ (without Br^- anion), TNP, and picrate were obtained by using B3LYP functional and 6-311+G(d,p) basis set. The DFT studies revealed that the energies of HOMO and LUMO of **BZQZPy**$^+$ are -8.459 eV and -6.504 eV, whereas, the energies of HOMO and LUMO of picrate are -3.424 eV and +0.1417 eV, respectively (**Figure 6.27**).

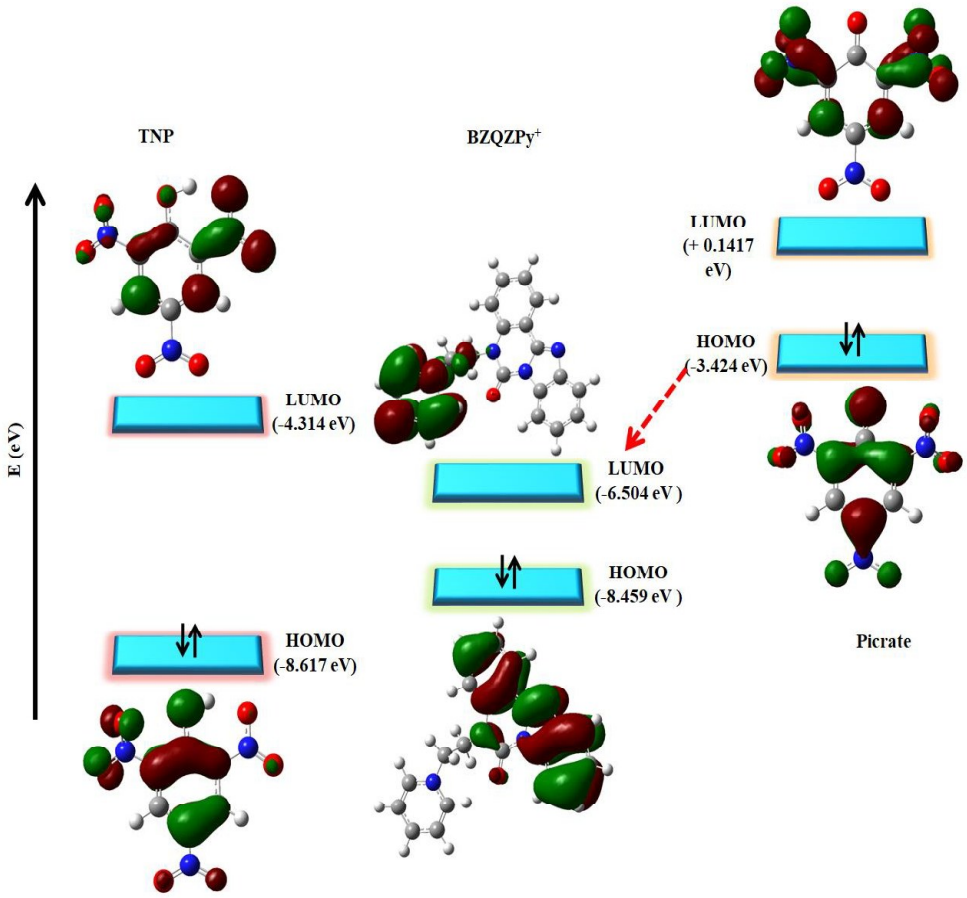

Figure 6.27 Pictorial representation of ground-state electron transfer from HOMO of picrate to LUMO of **BZQZPy**$^+$

These theoretical calculations indicate that the ground state electron transfer takes place from the HOMO of picrate to the LUMO of **BZQZPy**$^+$ and results in high quenching efficiency. HOMOs of other organic analytes were found to have low energy levels than the LUMO of **BZQZPy**$^+$ resulting in low quenching efficiency (**Figure 6.28**).

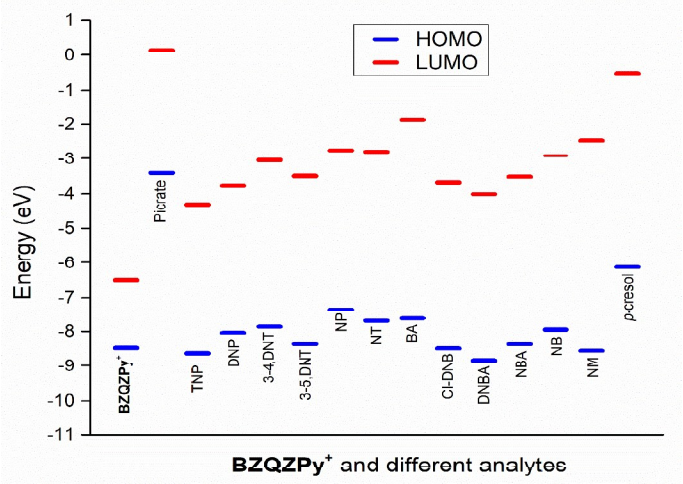

Figure 6.28 The LUMO-HOMO energy levels of **BZQZPy**$^{+}$ and organic analytes

The high sensitivity of **BZQZPy** towards TNP and the non-linear nature of the Stern-Volmer plot suggested that an energy transfer process may also be involved in the quenching process. There is a possibility of RET (resonance energy transfer) from the fluorophore **BZQZPy** (donor) to non-emissive TNP (acceptor) and the emission peak of the donor overlaps efficiently with the absorption band of the acceptor. [59] The maximum overlap between the absorption spectrum of TNP and the emission spectrum of **BZQZPy** resulted in more fluorescence quenching in comparison to the other organic analytes (**Figure 6.29**). To identify the extent of energy transfer, overlap integral (J_λ) and Förster distance (R_0) for **BZQZPy**-TNP interaction were calculated. The J_λ was found to be 1.13×10^{-12} M^{-1} cm^{-1} nm^4 and the low value of R_0 (13.61 Å) suggested RET to a very low extent [61].

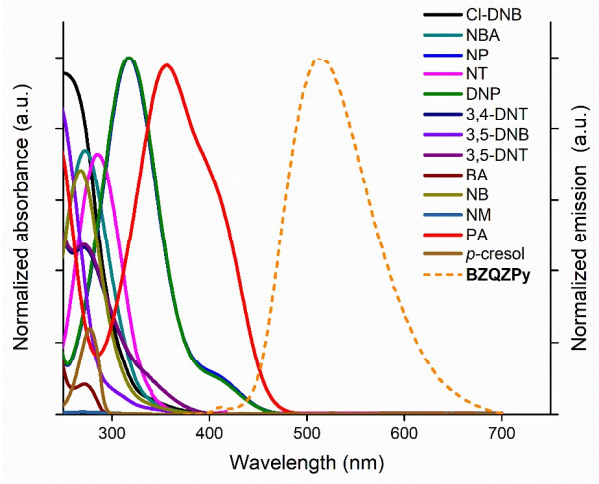

Figure 6.29 Absorption spectra of different organic analytes and emission spectra of the **BZQZPy** (10^{-4} M) in aqueous medium. UV-Visible spectra: solid line, Fluorescence spectra: dotted line

The lifetime experiment also suggested the possibility of the energy transfer mechanism. Fluorescence lifetime decay profiles showed a slight decrease in the lifetime of **BZQZPy**-TNP complex (3.73 ns) as compared to **BZQZPy** (4.70 ns) due to dynamic quenching (**Figure 6.30**).

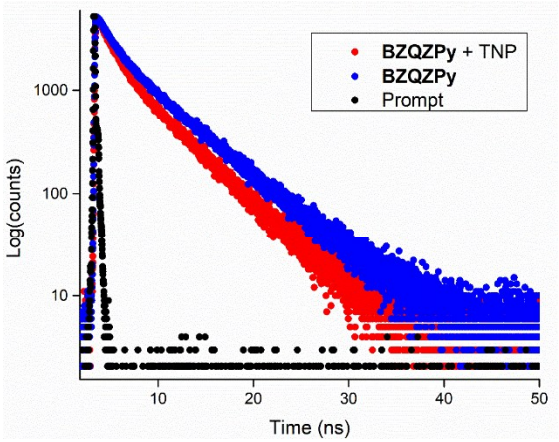

Figure 6.30 Lifetime decay profile of **BZQZPy** and **BZQZPy**-TNP

To inspect the binding mode between **BZQZPy** and TNP, ^{1}H NMR spectra was analyzed before and after the incremental addition of TNP to **BZQZPy** in DMSO-d_6 (**Figure 6.31**). A solution of **BZQZPy** containing 1 and 2 equiv. TNP showed a singlet of H_d at 8.50 and 8.58 ppm, respectively due to picrate anion, this signal in free TNP was observed at 8.60 ppm.

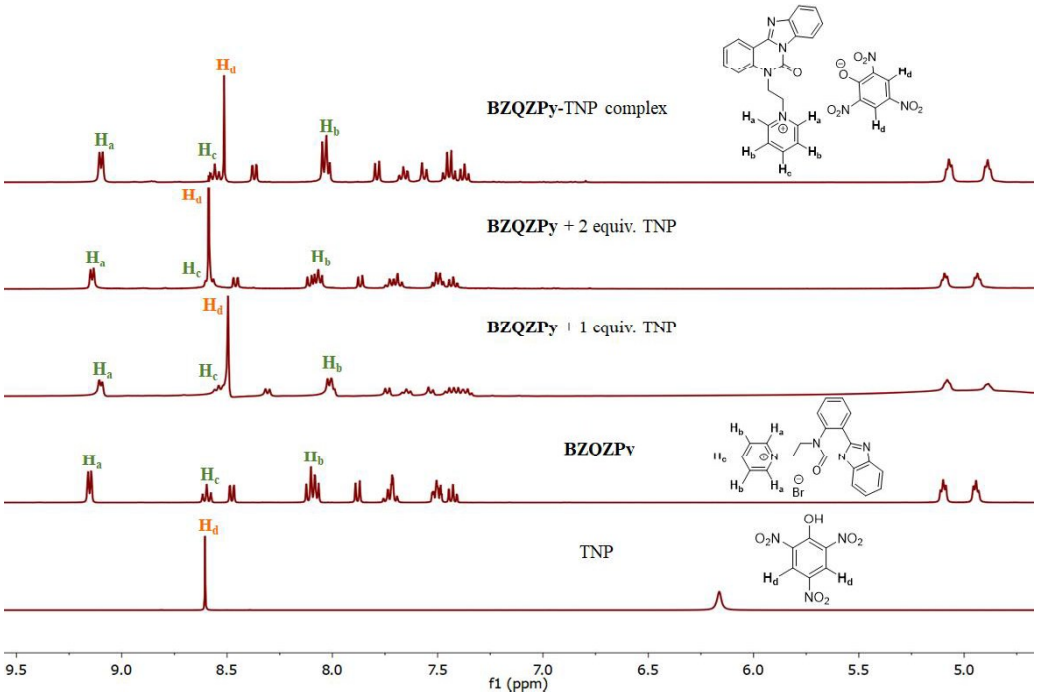

Figure 6.31 ^{1}H NMR spectra of **BZQZPy** with different equiv. of TNP (DMSO-d_6)

On addition of 1 equiv. of TNP, pyridinium proton signals H_a, H_b, and H_c in **BZQZPy** shifted to 9.09-9.10, 8.50, and 8.02 ppm, respectively, and the shifts were also observed for other aromatic and aliphatic protons. Furthermore, the reaction of **BZQZPy** with TNP in ethanol was performed and the final product **BZQZPy**-TNP complex (**Scheme 6.2**), was characterized by ^{1}H NMR spectrum (**Figure 6.32**). The proton signals of this product matched with the ^{1}H NMR pattern of **BZQZPy** with 1 equiv. of TNP. These observations support that **BZQZPy** interacts with TNP in a 1:1 molar ratio. In HRMS of **BZQZPy**-TNP complex, *m/z* peaks were observed in positive and negative mode at 341.1386 and 227.9897 for cationic [**BZQZPy**-Br]$^+$ and anionic [TNP-H]$^-$, respectively (**Figure 6.33**).

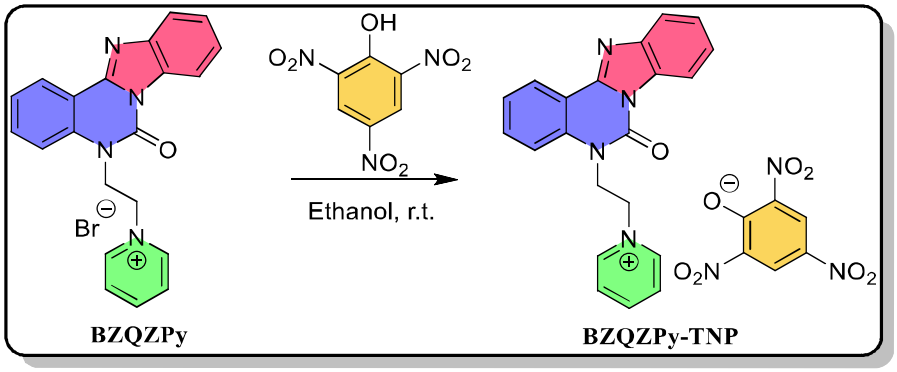

Scheme 6.2 Synthesis of **BZQZPy**-TNP complex

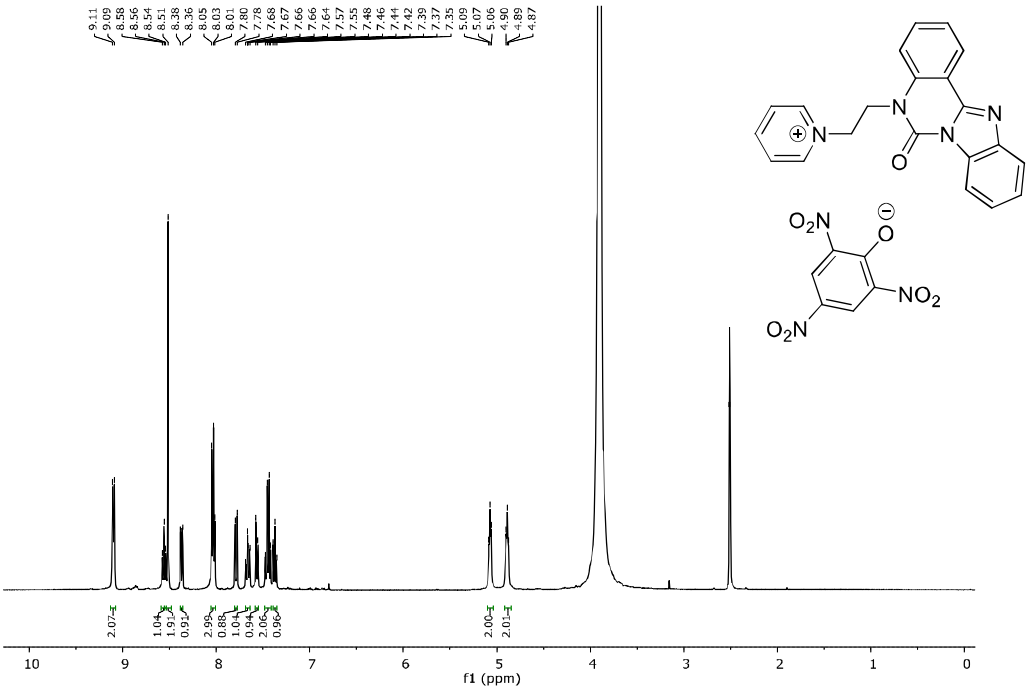

Figure 6.32 ^{1}H NMR spectrum of **BZQZPy-TNP** complex (DMSO-d_6)

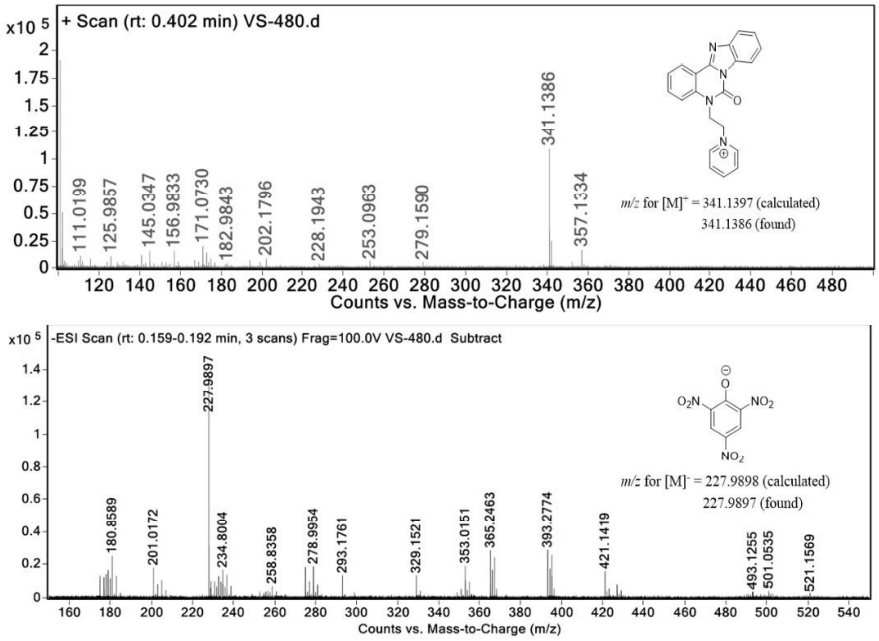

Figure 6.33 HRMS of **BZQZPy**-TNP complex

From the experimental and theoretical studies, it was concluded that the possible reasons for quenching are the formation of a ground state charge transfer complex as well as the excited state energy transfer processes, however, charge transfer is the predominant process.

6.2.4 Comparison of fluorescence quenching efficiency of TNP with NP and DNP

To elucidate the exceptional selectivity of **BZQZPy** towards TNP, a control experiment was performed using NP and DNP (**Figure 6.34**). The fluorescence quenching efficiency order was found to be TNP > DNP > NP which is same as their acidity order (TNP > DNP > NP). TNP being a strong acid (pK_a = 0.38), dissociates easily in aqueous medium and shows electrostatic interaction with cationic **BZQZPy**.

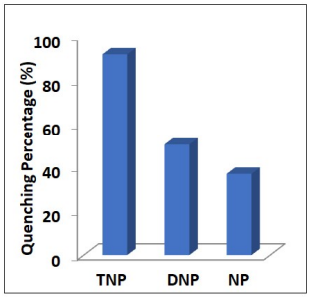

Figure 6.34 Comparison of percentage fluorescence quenching on the addition of TNP, DNP, and NP to the solution of **BZQZPy** in water

To check whether the quenching is due to the acidity of TNP, the fluorescence spectra of **BZQZPy** (10^{-4} M) was recorded with trifluoroacetic acid (TFA) which is more acidic than

TNP. TFA showed no effect on the emission intensity which contradicts the possibility of quenching by the acidity effect (**Figure 6.35**). The strong electrostatic interaction between **BZQZPy** and TNP with efficient charge transfer and energy transfer mechanisms are the responsible factors for this excellent fluorescence quenching [56].

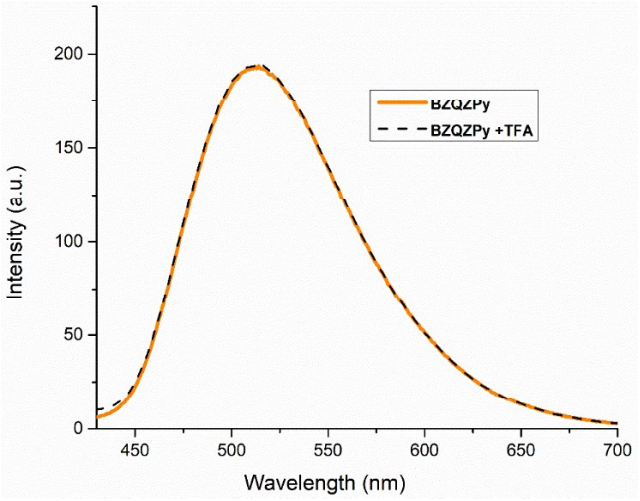

Figure 6.35 Fluorescence spectra of **BZQZPy** (10^{-4} M)before and after addition of TFA (trifluoroacetic acid)

6.2.5 Effect of pH

The pH-dependent sensing behaviour of **BZQZPy** was also studied and no change was observed in the fluorescence behaviour of **BZQZPy** at different pH suggesting its high stability under such conditions. The relative fluorescence intensity at 512 nm was measured before and after TNP addition at various pH. The maximum fluorescence quenching was found at low pH in the range 3-7. The decrease in the detection sensitivity at high pH may be attributed to less stability of **BZQZPy**-TNP complex (**Figure 6.36**).

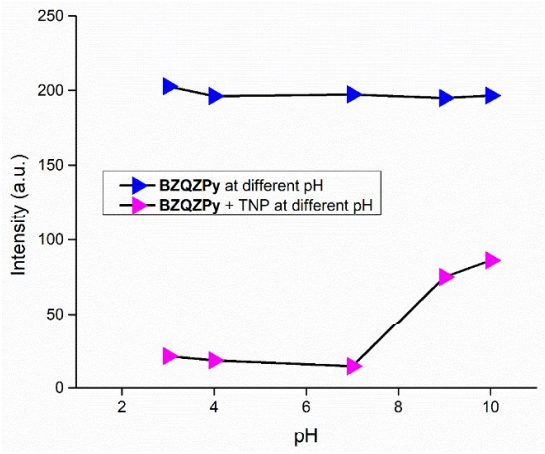

Figure 6.36 Change in the fluorescence spectrum of **BZQZPy** (10^{-4} M) before and after TNP addition under different pH conditions

6.2.6 Interference Study

To assess the interference of other analytes, fluorescence titrations of **BZQZPy** with TNP were performed in the presence of metal ions (Na^+, K^+, Ag^+, Mg^{2+}, Ca^{2+}, Mn^{2+}, Co^{2+}, Ni^{2+}, Cu^{2+}, Zn^{2+}, Cd^{2+}, Hg^{2+}, Pb^{2+}, Al^{3+}, Cr^{3+}, Fe^{3+}, La^{3+}, Eu^{3+}, Gd^{3+}, and Yb^{3+}), anions (F^-, Cl^-, Br^-, I^-, HSO_4^-, SO_4^-, and CH_3COO^-) and organic analytes (Cl-DNB, NBA, NP, NT, DNP, 3,4-DNT, DNBA, 3,5-DNT, BA, NB, NM, TNP, and *p*-cresol). No interference from metal ions, anions, and organic analytes was observed (**Figure 6.37a-c**).

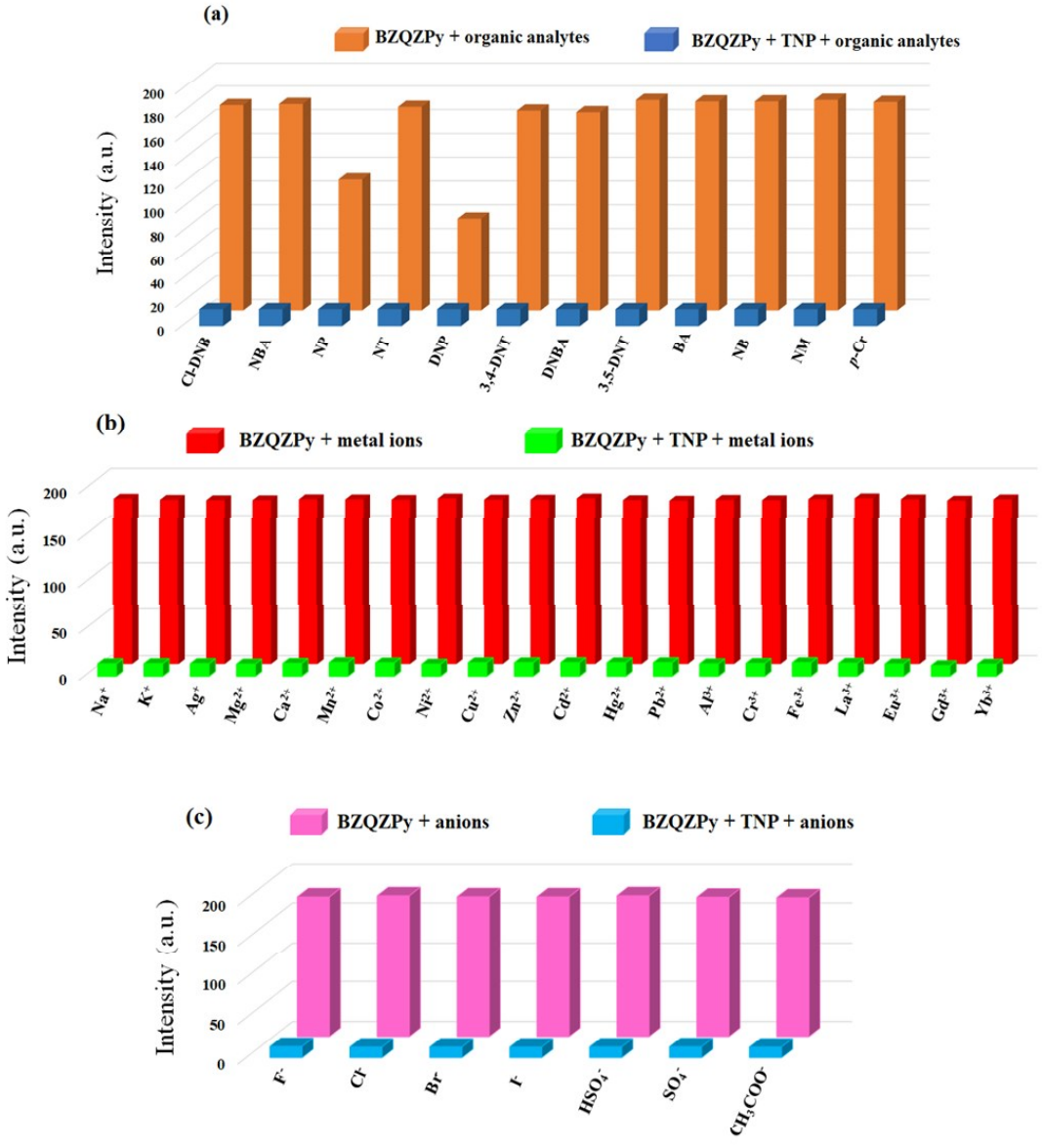

Figure 6.37 Fluorescence quenching efficiency of **BZQZPy** (10^{-4} M) with and without TNP after the addition of (**a**) organic analytes (**b**) metal ions and (**c**) anions

6.2.7 Contact mode detection of TNP

After successful detection of TNP in the solution phase, contact mode detection was executed, which is particularly advantageous in the field of analytical and forensic research. The filter paper test strips were prepared by dipping in an aqueous solution of **BZQZPy** (10^{-4} M) and dried in air. These test strips dipped in aqueous solutions of TNP (10^{-3}-10^{-6} M) after drying were visualized under a portable 365 nm UV lamp. The fluorescence quenching of **BZQZPy** (**Figure 6.38**) was observed and the detection limit was nearly 10^{-5} M of TNP.

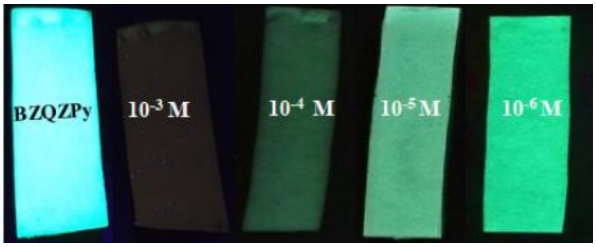

Figure 6.38 UV light visualization of filter paper strips containing **BZQZPy** before and after addition TNP (10^{-3}-10^{-6} M) under 365 nm UV lamp

6.2.8 Application in real water samples

To check the sensitivity and analytical performance, the detection of TNP in real water samples was also performed. The environmental water sample was obtained from the Ganga River (Rishikesh, India), the tap water sample was taken from our laboratory and the bottled mineral water was purchased from a local market. A series of water samples were prepared by spiking 20 μM standard TNP solution (**Figure 6.39**). Each experiment was repeated three times. The fluorescence intensity significantly decreased with the addition of TNP and the recovery was almost 100% (**Table 6.2**).

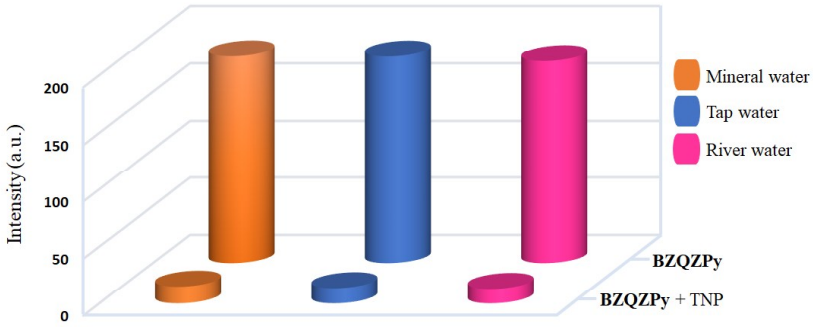

Figure 6.39 Fluorescence response of **BZQZPy** towards TNP in real water samples

Table 6.2 Detection of TNP in real water samples by **BZQZPy**

Sample	TNP spiked (μM)	TNP recovered, mean ± standard deviation (SD) (μM)	Recovery (%)
River water	20	19.93 ± 0.01	99.10
Tap water	20	19.87± 0.02	99.35
Mineral water	20	19.93± 0.06	99.67

4A.2.9 Comparison of BZQZPy with some of the previously reported TNP chemosensors

A comparative study of **BZQZPy** with some literature reported chemosensors for TNP detection are given in **Table 6.3**. It indicates that **BZQZPy** can detect TNP in a pure aqueous medium, whereas most of these listed probes needed toxic organic co-solvents. Low detection limit and real water sample monitoring are the other advantages of the proposed chemosensor.

Table 6.3 A comparative study of **BZQZPy** with some literature reported chemosensors for TNP detection

Solvent system	Detection limit	Quenching constant (K_{sv}) M^{-1}	Real sample analysis	References
H_2O	56 nM	3.866×10^4	Done	[73]
H_2O	208 nM	1.58×10^4	Done	[61]
pH 7.4 PBS-DMSO	0.067 ppb	8.34×10^6	-	[74]
H_2O-DMSO	10 pM	1.57×10^9	-	[65]
DMSO	NA	3.8×10^4, 3.3×10^4	-	[58]
H_2O-DMSO	10^{-14} M	6.25×10^5	-	[63]
CH_3CN	8.1×10^{-7} M	2.04×10^4	-	[59]
HEPES buffer-DMSO	1 nM 10 nM	3.57×10^5, 2.67×10^5	-	[62]
H_2O-DMSO	10^{-13} M	6.73×10^8	-	[71]
H_2O-DMSO	5×10^{-13} M	1.20×10^{11}	-	[64]
H_2O-THF	2.12×10^{-8} M	3.57×10^4	Done	[75]
DMSO	700 ppt	-	-	[45]
H_2O	20 nM	1.53×10^4	Done	Present work

6.3 Experimental

6.3.1 Synthesis of 1-(2-bromoethyl)-1H-indole-2,3-dione

The 1-(2-bromoethyl)-1H-indole-2,3-dione was synthesized according to the reported method [72]. A solution containing 1H-indole-2,3-dione (10 g, 0.068 mol) and K_2CO_3 (18.9 g, 0.102 mol) in DMF was stirred for 15 min, thereafter 1,2-dibromoethane (255.5 g, 1.36 mol, 117.2 mL) was added. After stirring at room temperature for 2 h, the reaction mixture was filtered and washed with DMF and filtrate was evaporated under reduced pressure. The crude purified by column chromatography with hexanes and ethyl acetate eluents provided 1-(2-bromoethyl)-1H-indole-2,3-dione (**Scheme 6.1**).

6.3.2 Synthesis of 1-(2-(2,3-dioxoindolin-1-yl)ethyl)pyridin-1-ium bromide (IPy)

The reaction of pyridine (1.5 equiv.) with 1-(2-bromoethyl)-1H-indole-2,3-dione (discussed in chapter 2, section 2.4.3) (1 equiv.) at 70 °C for 8 h afforded orange viscous liquid. Crude was washed with diethyl ether and ethyl acetate, obtained yellow solid was filtered and dried to afford **IPy** (**Scheme 6.1**).

6.3.3 Synthesis of 1-(2-(6-oxobenzo[4,5]imidazo[1,2-c]quinazolin-5(6H)-yl)ethyl)pyridin-1-ium bromide (BZQZPy)

IPy (1 equiv.) was stirred in methanol and refluxed for 15 min. A methanolic solution of *o*-phenylenediamine (2 equiv.) was added to it and the mixture was refluxed for 10 h. The reaction mixture was evaporated and washed with ethyl acetate and methanol. Obtained pale-yellow solid was dried under vacuum ((**Scheme 6.1**)). Yield: 85%; mp: 181-185 °C.

6.3.4 Synthesis of BZQZPy-TNP complex

To a solution of compound **BZQZPy** (1 equiv.) in ethanol, an ethanolic solution of TNP (5 equiv.) was added dropwise at room temperature. The reaction mixture was stirred for 6 h, the yellow precipitate obtained was filtered and washed with ethanol (**Scheme 6.2**).

6.3.5 Physical and spectral data of synthesized compounds

1-(2-bromoethyl)-1H-indole-2,3-dione

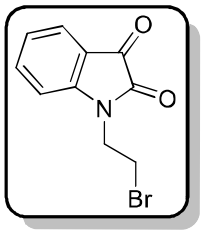

Anacarat solid (82%); mp: 132-133 °C; ^{1}H NMR (400 MHz, $CDCl_3$) δ 7.66-7.61 (m, 2H), 7.17 (td, *J* = 7.6 Hz, 1H), 7.03 (dd, *J* = 7.6 Hz, 1H), 4.17 (t, *J* = 6.7 Hz, 2H), 3.63 (t, *J* = 6.7 Hz, 2H). ^{13}C NMR (100 MHz, $CDCl_3$) δ 186.9, 161.0, 150.2, 137.2, 136.4, 123.4, 121.6, 116.3, 45.0, 30.9.

1-(2-(2,3-dioxoindolin-1-yl)ethyl)pyridin-1-ium bromide (IPy)

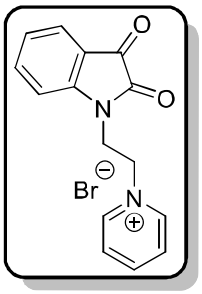

Yellow solid (90%); mp: 175-177 °C; ^{1}H NMR (400 MHz, DMSO-d_6) δ 9.21 (d, J = 5.8 Hz, 2H), 8.62 (t, J = 7.8 Hz, 1H), 8.12 (t, J = 7.0 Hz, 2H), 7.63 (t, J = 7.7 Hz, 1H), 7.57 (d, J = 7.3 Hz, 1H), 7.17 (m, 2H), 4.94 (t, J = 5.1 Hz, 2H), 4.33 (t, J = 5.2 Hz, 2H); ^{13}C NMR (100 MHz, DMSO-d_6) δ 182.9, 159.1, 150.3, 146.5, 146.1, 138.5, 128.5, 125.0, 124.1, 118.3, 111.0, 59.3, 41.5. HRMS (ESI): *m/z* calcd for $[C_{15}H_{13}N_2O_2]^+$ [**IPy** - Br]$^+$ 253.0972, found 253.0967.

1-(2-(6-oxobenzo[4,5]imidazo[1,2-c]quinazolin-5(6H)-yl)ethyl)pyridin-1-ium bromide (BZQZPy)

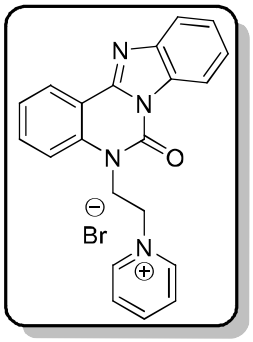

Pale-yellow solid (85%); mp: 181-185 °C; ^{1}H NMR (400 MHz, DMSO-d_6) δ 9.15 (d, J = 5.3 Hz, 2H), 8.60 (t, J = 7.8 Hz, 1H), 8.48 (dd, J = 7.9, 1.2 Hz, 1H), 8.14-8.05 (m, 3H), 7.88 (d, J = 8.0 Hz, 1H), 7.76-7.68 (m, 2H), 7.54-7.47 (m, 2H), 7.45-7.40 (m, 1H), 5.10 (t, J = 5.2 Hz, 2H), 4.94 (t, J = 5.1 Hz, 2H); ^{13}C NMR (100 MHz, DMSO-d_6) δ 147.4, 147.3, 146.4, 146.2, 143.9, 137.6, 133.1, 131.2, 128.4, 125.8, 125.7, 124.5, 124.4, 119.7, 115.6, 115.2, 113.6, 59.6, 44.3. HRMS (ESI): *m/z* calcd for $[C_{21}H_{17}N_4O]^+$ [**BZQZPy** - Br]$^+$ 341.1397, found 341.1388.

BZQZPy-TNP complex

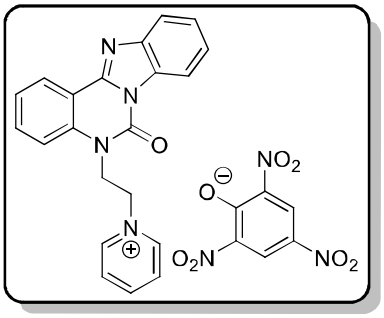

Yellow solid (95%); mp: 210-211 °C; ^{1}H NMR (400 MHz, DMSO-d_6) δ 9.10 (d, J = 6.1 Hz, 2H), 8.56 (t, J = 7.8 Hz, 1H), 8.51 (s, 2H), 8.37 (d, J = 9.4 Hz, 1H), 8.03 (t, J = 7.1 Hz, 3H), 7.79 (d, J = 7.9 Hz, 1H), 7.69-7.64 (m, 1H), 7.56 (d, J = 8.5 Hz, 1H), 7.45 (q, J = 7.9, 7.3 Hz, 2H), 7.37 (t, J = 8.1 Hz, 1H), 5.07 (t, J = 5.2 Hz, 2H), 4.89 (t, J = 5.2 Hz, 2H). HRMS (ESI): *m/z* calcd for $[C_{21}H_{17}N_4O]^+$ [**BZQZPy** - Br]$^+$ 341.1397, found 341.1386 and *m/z* calcd for $[C_6H_2N_3O_7]^-$ [TNP - H]$^-$ 227.9898, found 227.9897.

6.4 Conclusions

In this study by utilizing a simple synthetic strategy, a hydrophilic pyridinium-based benzimidazo-quinazolinone chemosensor was synthesized. **BZQZPy** worked as a sensitive

and selective fluorescence turn-off chemosensor for the detection of TNP in a pure aqueous medium. The experimental and theoretical studies indicate that ground state charge transfer complex formation and energy transfer mechanisms are responsible for the fluorescence quenching of **BZQZPy** by TNP. The chemosensor was also tested for the detection of TNP on filter paper strips and in real water samples. The satisfactory results indicate that **BZQZPy** can be a good choice for TNP detection in real water samples.

6.5 References

[1] Jigyasa; Kumar, D.; Arora, P.; Singh, H.; Rajput, J. K. *Spectrochimica Acta Part A: Molecular and Biomolecular Spectroscopy* **2020**, *230*, 118087-118097.

[2] Chio, W.-I. K.; Peveler, W. J.; Assaf, K. I.; Moorthy, S.; Nau, W. M.; Parkin, I. P.; Olivo, M.; Lee, T.-C. *The Journal of Physical Chemistry C* **2019**, *123*, 15769-15776.

[3] Han, T.; Kang, H.; Yuan, Y.; Zhang, Y.; Dong, L. *Spectrochimica Acta Part A: Molecular and Biomolecular Spectroscopy* **2020**, 118243-118251.

[4] Zhao, Y.; Pan, M.; Liu, F.; Liu, Y.; Dong, P.; Feng, J.; Shi, T.; Liu, X. *Analytica Chimica Acta* **2020**, *1106*, 133-138.

[5] Fuller, M. E.; Koster van Groos, P. G.; Jarrett, M.; Kucharzyk, K. H.; Minard-Smith, A.; Heraty, L. J.; Sturchio, N. C. *Chemosphere* **2020**, *250*, 126210-126217.

[6] Thomas, J. L.; Donnelly, C. C.; Lloyd, E. W.; Mothershead, R. F.; Miller, M. L. *Forensic Science International* **2018**, *284*, 65-77.

[7] Shanmugaraju, S.; Dabadie, C.; Byrne, K.; Savyasachi, A. J.; Umadevi, D.; Schmitt, W.; Kitchen, J. A.; Gunnlaugsson, T. *Chemical Science* **2017**, *8*, 1535-1546.

[8] Areti, S.; Bandaru, S.; Kandi, R.; Rao, C. P. *ACS Omega* **2019**, *4*, 1167-1177.

[9] Nagarkar, S. S.; Desai, A. V.; Ghosh, S. K. *CrystEngComm* **2016**, *18*, 2994-3007.

[10] Chahal, M. K.; Sankar, M. *Analytical Methods* **2015**, *7*, 10272-10279.

[11] Pandith, A.; Kumar, A.; Lee, J.-Y.; Kim, H.-S. *Tetrahedron Letters* **2015**, *56*, 7094-7099.

[12] Kundu, B. K.; Pragti; Reena; Mobin, S. M.; Mukhopadhyay, S. *New Journal of Chemistry* **2019**, *43*, 11483-11492.

[13] Roberts, A. G.; Gregor, W.; Britt, R. D.; Kramer, D. M. *Biochimica et Biophysica Acta (BBA) - Bioenergetics* **2003**, *1604*, 23-32.

[14] Hu, H.; Wang, F.; Yu, L.; Sugimura, K.; Zhou, J.; Nishio, Y. *ACS Sustainable*

Chemistry & Engineering **2018**, *6*, 1436-1445.

[15] Adil, L. R.; Gopikrishna, P.; Krishnan Iyer, P. *ACS Applied Materials & Interfaces* **2018**, *10*, 27260-27268.

[16] Tanwar, A. S.; Patidar, S.; Ahirwar, S.; Dehingia, S.; Iyer, P. K. *Analyst* **2019**, *144*, 669-676.

[17] Pinrat, O.; Boonkitpatarakul, K.; Paisuwan, W.; Sukwattanasinitt, M.; Ajavakom, A. *Analyst* **2015**, *140*, 1886-1893.

[18] Ma, J.; Lin, T.; Pan, X.; Wang, W. *Chemistry of Materials* **2014**, *26*, 4221-4229.

[19] Nandi, S. K.; Roy Chowdhury, S.; Podder, D.; Ghorai, P. K.; Haldar, D. *Crystal Growth & Design* **2020**, *20*, 1884-1890.

[20] Qiu, F.; Huang, Y.-H.; Ge, Q.; Liu, M.; Cong, H.; Tao, Z. *Spectrochimica Acta Part A: Molecular and Biomolecular Spectroscopy* **2020**, *226*, 117583-117590.

[21] Ye, D.-Y.; Dong, Z.-Y.; Pu, Y.-Q.; Huang, G.-W.; An, Y.; Lü, C.-W. *Dyes and Pigments* **2020**, *174*, 108016-108024.

[22] Pan, J.; Tang, F.; Ding, A.; Kong, L.; Yang, L.; Tao, X.; Tian, Y.; Yang, J. *RSC Advances* **2015**, *5*, 191-195.

[23] Shanmugaraju, S.; Mukherjee, P. S. *Chemistry – A European Journal* **2015**, *21*, 6656-6666.

[24] Geethanjali, H. S.; Nagaraja, D.; Melavanki, R. M. *Journal of Molecular Liquids* **2015**, *209*, 669-675.

[25] Sun, X.; Wang, Y.; Lei, Y. *Chemical Society Reviews* **2015**, *44*, 8019-8061.

[26] Wallace, B.; Atzberger, P. J. *PLOS ONE* **2017**, *12*, e0177122.

[27] Salinas, Y.; Martínez-Máñez, R.; Marcos, M. D.; Sancenón, F.; Costero, A. M.; Parra, M.; Gil, S. *Chemical Society Reviews* **2012**, *41*, 1261-1296.

[28] Ponnuvel, K.; Banuppriya, G.; Padmini, V. *Sensors and Actuators B: Chemical* **2016**, *234*, 34-45.

[29] Santra, D. C.; Bera, M. K.; Sukul, P. K.; Malik, S. *Chemistry – A European Journal* **2016**, *22*, 2012-2019.

[30] Toal, S. J.; Trogler, W. C. *Journal of Materials Chemistry* **2006**, *16*, 2871-2883.

[31] Dong, W.; Fei, T.; Palma-Cando, A.; Scherf, U. *Polymer Chemistry* **2014**, *5*, 4048-4053.

[32] Geng, T.; Zhu, Z.; Wang, X.; Xia, H.; Wang, Y.; Li, D. *Sensors and Actuators B: Chemical* **2017**, *244*, 334-343.

[33] Mukherjee, S.; Desai, A. V.; Manna, B.; Inamdar, A. I.; Ghosh, S. K. *Crystal Growth & Design* **2015**, *15*, 4627-4634.

[34] Han, Y.; Cao, H.-T.; Sun, H.-Z.; Shan, G.-G.; Wu, Y.; Su, Z.-M.; Liao, Y. *Journal of Materials Chemistry C* **2015**, *3*, 2341-2349.

[35] Cui, Y.; Wen, L.-L.; Shan, G.-G.; Sun, H.-Z.; Mao, H.-T.; Zhang, M.; Su, Z.-M. *Sensors and Actuators B: Chemical* **2017**, *244*, 314-322.

[36] Kumar, A.; Kumar, A.; Pandey, D. S. *Dalton Transactions* **2016**, *45*, 8475-8484.

[37] Lin, L.; Rong, M.; Lu, S.; Song, X.; Zhong, Y.; Yan, J.; Wang, Y.; Chen, X. *Nanoscale* **2015**, *7*, 1872-1878.

[38] Wang, H.; Chen, C.; Liu, Y.; Wu, Y.; Yuan, Y.; Zhou, Q. *Talanta* **2019**, *198*, 242-248.

[39] Sk, M. P.; Chattopadhyay, A. *RSC Advances* **2014**, *4*, 31994-31999.

[40] Chen, S.; Song, Y.; Shi, F.; Liu, Y.; Ma, Q. *Sensors and Actuators B: Chemical* **2016**, *231*, 634-640.

[41] Champagne, P.-L.; Kumar, R.; Ling, C.-C. *Sensors and Actuators B: Chemical* **2019**, *281*, 229-238.

[42] Wang, L.; Cui, M.; Tang, H.; Cao, D. *Dyes and Pigments* **2018**, *155*, 107-113.

[43] Bhalla, V.; Gupta, A.; Kumar, M.; Rao, D. S. S.; Prasad, S. K. *ACS Applied Materials & Interfaces* **2013**, *5*, 672-679.

[44] Wu, Y.-C.; Luo, S.-H.; Cao, L.; Jiang, K.; Wang, L.-Y.; Xie, J.-C.; Wang, Z.-Y. *Analytica Chimica Acta* **2017**, *976*, 74-83.

[45] Nath, S.; Pathak, S. K.; Pradhan, B.; Gupta, R. K.; Reddy, K. A.; Krishnamoorthy, G.; Achalkumar, A. S. *New Journal of Chemistry* **2018**, *42*, 5382-5394.

[46] Cao, X.; Zhao, N.; Lv, H.; Ding, Q.; Gao, A.; Jing, Q.; Yi, T. *Langmuir* **2017**, *33*, 7788-7798.

[47] Alam, P.; Kaur, G.; Kachwal, V.; Gupta, A.; Roy Choudhury, A.; Laskar, I. R. *Journal of Materials Chemistry C* **2015**, *3*, 5450-5456.

[48] Bhalla, V.; Gupta, A.; Kumar, M. *Organic Letters* **2012**, *14*, 3112-3115.

[49] Gupta, M.; Lee, H.-i. *ACS Applied Materials & Interfaces* **2018**, *10*, 41717-41723.

[50] Kaur, I.; Sharma, V.; Mobin, S. M.; Kaur, P.; Singh, K. *Sensors and Actuators B: Chemical* **2019**, *281*, 613-622.

[51] Feng, H.-T.; Zheng, Y.-S. *Chemistry A European Journal* **2014**, *20*, 195-201.

[52] Arockiam, J. B.; Ayyanar, S. *Sensors and Actuators B: Chemical* **2017**, *242*, 535-544.

[53] Park, M. J.; Lee, J. K.; Lee, B. S.; Lee, Y.-W.; Choi, I. S.; Lee, S.-g. *Chemistry of*

Materials **2006**, *18*, 1546-1551.

[54] Xu, J.; Li, Q.; Yue, Y.; Guo, Y.; Shao, S. *Biosensors and Bioelectronics* **2014**, *56*, 58-63.

[55] Bishnoi, S.; Milton, M. D. *Journal of Photochemistry and Photobiology A: Chemistry* **2017**, *335*, 52-58.

[56] Hussain, S.; Malik, A. H.; Afroz, M. A.; Iyer, P. K. *Chemical Communications* **2015**, *51*, 7207-7210.

[57] Ding, L.; Bai, Y.; Cao, Y.; Ren, G.; Blanchard, G. J.; Fang, Y. *Langmuir* **2014**, *30*, 7645-7653.

[58] Roy, B.; Bar, A. K.; Gole, B.; Mukherjee, P. S. *The Journal of Organic Chemistry* **2013**, *78*, 1306-1310.

[59] Tian, X.; Qi, X.; Liu, X.; Zhang, Q. *Sensors and Actuators B: Chemical* **2016**, *229*, 520-527.

[60] Kumari, S.; Joshi, S.; Cordova-Sintjago, T. C.; Pant, D. D.; Sakhuja, R. *Sensors and Actuators B: Chemical* **2016**, *229*, 599-608.

[61] Joshi, S.; Kumari, S.; Chamorro, E.; Pant, D. D.; Sakhuja, R. *ChemistrySelect* **2016**, *1*, 1756-1762.

[62] Kumar, R.; Sandhu, S.; Singh, P.; Hundal, G.; Hundal, M. S.; Kumar, S. *Asian Journal of Organic Chemistry* **2014**, *3*, 805-813.

[63] Sandhu, S.; Kumar, R.; Singh, P.; Kumar, S. *Journal of Materials Chemistry C* **2016**, *4*, 3209-3216.

[64] Sandhu, S.; Kumar, R.; Singh, P.; Mahajan, A.; Kaur, M.; Kumar, S. *ACS Applied Materials & Interfaces* **2015**, *7*, 10491-10500.

[65] Tripathi, N.; Sandhu, S.; Singh, P.; Mahajan, A.; Kaur, M.; Kumar, S. *Sensors and Actuators B: Chemical* **2016**, *231*, 79-87.

[66] Sowmiah, S.; Esperança, J. M. S. S.; Rebelo, L. P. N.; Afonso, C. A. M. *Organic Chemistry Frontiers* **2018**, *5*, 453-493.

[67] Wu, D.; Yu, Y.; Zhang, J.; Guo, L.; Kong, Y. *ACS Applied Materials & Interfaces* **2018**, *10*, 23362-23368.

[68] Zhang, C.; Zhang, H.; Li, M.; Zhou, Y.; Zhang, G.; Shi, L.; Yao, Q.; Shuang, S.; Dong, C. *Talanta* **2019**, *197*, 218-224.

[69] Ghosh, K.; Sarkar, A. R.; Samadder, A.; Khuda-Bukhsh, A. R. *Organic Letters* **2012**, *14*, 4314-4317.

[70] Wang, D.-H.; Gong, Z.; Sun, R.; Zhao, D.-Z.; Yang, Z.-X. *RSC Advances* **2015**, *5*, 44824-44827.

[71] Tripathi, N.; Singh, P.; Kumar, S. *New Journal of Chemistry* **2017**, *41*, 8739-8747.

[72] Feng, L.-S.; Liu, M.-L.; Wang, B.; Chai, Y.; Hao, X.-Q.; Meng, S.; Guo, H.-Y. *European Journal of Medicinal Chemistry* **2010**, *45*, 3407-3412.

[73] Luo, T.; Li, Y.; Xu, Y.; Zhang, S.; Wang, Y.; Kou, X.; Xiao, D. *Sensors and Actuators B: Chemical* **2017**, *253*, 231-238.

[74] Kumar, A.; Pandith, A.; Kim, H.-S. *Sensors and Actuators B: Chemical* **2016**, *231*, 293-301.

[75] Jiang, K.; Luo, S.-H.; Pang, C.-M.; Wang, B.-W.; Wu, H.-Q.; Wang, Z.-Y. *Dyes and Pigments* **2019**, *162*, 367-376.